

# Mechanical Systems and Signal Processing

## On the Investigation of Ash Deposition Effect on Flow-Induced Vibration Energy Harvesting

--Manuscript Draft--

<b>Manuscript Number:</b>	MSSP21-3265R2
<b>Article Type:</b>	Standard Research Article
<b>Keywords:</b>	ash deposition; energy harvesting; flow-induced vibration; galloping; vortex-induced vibration
<b>Corresponding Author:</b>	Guobiao Hu, Ph.D. Nanyang Technological University SINGAPORE
<b>First Author:</b>	Junlei Wang, PhD
<b>Order of Authors:</b>	Junlei Wang, PhD
	Shanghao Gu, PhD
	Daniil Yurchenko, PhD
	Guobiao Hu, Ph.D.
	Ronghan Wei, PhD
<b>Abstract:</b>	<p>This paper proposes harnessing the aerokinetic energy in flue systems and it explores the effect of the ash deposition on flow-induced vibration energy harvesting performance. Bell-shaped and horn-like bluff bodies are designed to simulate different ash depositions on a conventional elliptic cylinder bluff body. Wind tunnel experiments were conducted to investigate the energy harvesting performance using different ash deposition distributed over the bluff bodies. The experimental results show that compared to the baseline model of a conventional elliptic cylinder bluff body, the bell-shaped bluff body suppresses the flow-induced vibration and deteriorates the energy harvesting performance. In contrast, the horn-like bluff body can benefit energy harvesting by reducing the galloping cut-in wind speed and increasing the voltage output. The voltage output of an optimal prototype using the horn-like bluff body is increased by 516%. Computational fluid dynamics (CFD) simulations were carried out to unveil the physical mechanisms behind the phenomena. The CFD analysis results indicate that the appearance of the small-scale secondary vortices (SV) widens the wake flow and increases the aerodynamic force produced by the horn-like bluff body. The flow-induced vibration of the harvester using the horn-like bluff body transforms from VIV to galloping. Therefore, it has been preliminarily demonstrated that the unfavorable ash deposition phenomenon in flue systems has the potential for promoting flow-induced vibration energy harvesting.</p>

Dear Editors of Mechanical Systems and Signal Processing:

We would like to submit our manuscript entitled “*On the Investigation of Ash Deposition Effect on Flow-Induced Vibration Energy Harvesting*” for possible publication in Mechanical Systems and Signal Processing. We declare that there is no conflict of interest between the authors, and this is an original work that has not been published previously and is not under consideration for publication elsewhere, in whole or in part.

This paper proposes to install a flow-induced piezoelectric energy harvester (FIVPEH) in flues or heat exchange systems where aerokinetic energy exists. Ash deposition is an inevitable phenomenon during the combustion process. Therefore, the ash deposition on the elliptic cylinder bluff body is considered, and its effect on the energy harvesting performance is investigated. According to the ash deposition types summarized in the literature, bell-shaped and horn-shaped cylinder bluff bodies are designed to consider the ash deposition effect on a conventional elliptic cylinder bluff body. Wind tunnel experiments are conducted to investigate the energy harvesting performance using different ash deposition attached bluff bodies. It has been found that though the ash deposition of dusty flue gas in the boiler and heat exchanger often threatens the safety of the equipment and affects the heat exchange performance, horn-like ash deposition formed on the elliptic cylinder bluff body can benefit energy harvesting by reducing the cut-in wind speed and increasing the voltage output. Computational fluid dynamics (CFD) simulations are carried out to explain the physical mechanisms behind the phenomena.

We deeply appreciate your consideration of our manuscript and look forward to receiving comments from the reviewers. If you have any queries, please don't hesitate to contact us.

Thank you and best regards.

Yours sincerely,

Corresponding author: Dr. Guobiao Hu

E-mail: [guobiao.hu@ntu.edu.sg](mailto:guobiao.hu@ntu.edu.sg)

## Responses to review comments

We are thankful for the time and efforts of the editor and reviewers. The review comments are valuable for us to improve the quality of our manuscript. We have considered and addressed all the comments from the reviewers, and the detailed point-to-point response is given below in red. The changes in the revised manuscript are highlighted in yellow.

### **Reviewer #1:**

The authors have responded adequately to my concerns on the original submission, and they have made appropriate revisions to the paper. I therefore recommend acceptance of the paper for publication in MSSP.

While reading the paper, I have made a number of linguistic corrections and improvements, which may be found in the attached marked typescript, for the authors to consider/implement.

**Response:** Thanks to the reviewer for recommending our paper. We sincerely appreciate that the reviewer has made a number of linguistic corrections and improvements. We have made corresponding modifications in the revised manuscript by following the typescript from the reviewer.

# On the Investigation of Ash Deposition Effect on Flow-Induced Vibration Energy Harvesting

Junlei Wang<sup>1</sup>, Shanghao Gu<sup>1</sup>, Daniil Yurchenko<sup>2</sup>, Guobiao Hu<sup>3,4\*</sup>, Ronghan Wei<sup>5,6</sup>

<sup>1</sup> School of Mechanical and Power Engineering, Zhengzhou University, Zhengzhou 450000, China

<sup>2</sup> Institute of Sound and Vibration Research, University of Southampton, Southampton, SO17 1BJ, UK.

<sup>3</sup> School of Civil and Environmental Engineering, Nanyang Technological University, 50 Nanyang Avenue, 639798, Singapore

<sup>4</sup> State Key Laboratory of Structural Analysis for Industrial Equipment, Dalian University of Technology, Dalian 116024, China

<sup>5</sup> School of Mechanics and Safety Engineering, Zhengzhou University, Zhengzhou 450000, China

<sup>6</sup> China Institute of Intelligent Sensing, Zhengzhou University, Zhengzhou 450000, China

\*Corresponding author: [guobiao.hu@ntu.edu.sg](mailto:guobiao.hu@ntu.edu.sg)

## Abstract

This paper proposes harnessing the aerokinetic energy in flue systems and it explores the effect of the ash deposition on flow-induced vibration energy harvesting performance. Bell-shaped and horn-like bluff bodies are designed to simulate different ash depositions on a conventional elliptic cylinder bluff body. Wind tunnel experiments were conducted to investigate the energy harvesting performance using different ash deposition distributed over the bluff bodies. The experimental results show that compared to the baseline model of a conventional elliptic cylinder bluff body, the bell-shaped bluff body suppresses the flow-induced vibration and deteriorates the energy harvesting performance. In contrast, the horn-like bluff body can benefit energy harvesting by reducing the galloping cut-in wind speed and increasing the voltage output. The voltage output of an optimal prototype using the horn-like bluff body is increased by 516%. Computational fluid dynamics (CFD) simulations were carried out to unveil the physical mechanisms behind the phenomena. The CFD analysis results indicate that the appearance of the small-scale secondary vortices (SV) widens the wake flow and increases the aerodynamic force produced by the horn-like bluff body. The flow-induced vibration of the harvester using the horn-like bluff body transforms from VIV to galloping. Therefore, it has been preliminarily demonstrated that the unfavorable ash deposition phenomenon in flue systems has the potential for promoting flow-induced vibration energy harvesting.

1 **Keywords:** ash deposition, energy harvesting, flow-induced vibration, galloping  
2  
3 vortex-induced vibration  
4

## 5 **1. Introduction**

6  
7  
8 In recent years, low-power consumption devices have been massively used in  
9 various fields to develop the Internet of Things (IoTs) [1, 2]. Most of these devices are  
10 powered by traditional chemical batteries. However, they often have limited storage  
11 capacities but bulky volumes. In some particular scenarios, such as remote areas,  
12 underwater environments, implant health monitoring, batteries are difficult to replace  
13 and maintain [3]. Therefore, harvesting energy from the ambient environment to  
14 provide the necessary power supply becomes a suitable battery-free solution to  
15 address the above issue. Common natural sources that are widely accessible in our  
16 ambient environment include solar energy [4, 5], vibration energy [6], wind energy [7,  
17 8], and wave energy [9, 10]. Vibration energy harvesting refers to the technique of  
18 converting vibration energy into electrical energy through piezoelectric [11-13],  
19 electromagnetic [14, 15], or electrostatic [16, 17] transduction mechanisms. Due to  
20 the advantages of high power density, simple structure, and long service life,  
21 piezoelectric energy harvesting has attracted lots of research interest [18, 19].  
22  
23

24  
25 Flow-induced vibration (FIV) is a natural phenomenon that ubiquitously exists in  
26 our ambient environment. Therefore, FIV-based energy harvesting technology has  
27 been extensively developed in recent years [20]. FIV phenomena can be further  
28 classified into vortex-induced vibration (VIV) [21], galloping [22], flutter [23, 24],  
29 and wake galloping [25]. VIV-based piezoelectric energy harvesters (VIVPEH) can  
30 efficiently generate considerable power in the lock-in region. However, when the flow  
31 velocity exceeds the lock-in region, the structural vibration will decrease significantly,  
32 and the energy harvesting performance will deteriorate dramatically. Researchers have  
33 devoted numerous efforts to improving the performance of VIVPEH. Akaydin *et al.*  
34 [26] designed a VIVPEH by connecting a cantilever beam to a cylindrical bluff body.  
35 The wind tunnel test showed that the designed VIVPEH could generate approximately  
36 a power of 0.1 mW at a wind speed of 1.192 m/s. Dai *et al.* [27] established a  
37 nonlinear distributed-parameter model for a VIVPEH. They discussed the influences  
38 of the bluff body, the piezoelectric sheet length, and the electrical resistance on the  
39 synchronization region and the performance of the harvester. Azadeh-Ranjba *et al.* [28]  
40 investigated the influence of the aspect ratio of the rigid cylinder on a VIVPEH. The  
41 results indicated that an appropriate aspect ratio could not only increase the power  
42 output of the VIVPEH but also broaden its lock-in region. In recent years, researchers  
43 have been showing interest in optimizing the surface structure of the bluff body to  
44 widen the lock-in region of a VIVPEH for broadband energy harvesting. For example,  
45 Hu *et al.* [29] added two rods to a circular cylinder bluff body of a VIVPEH to alter  
46 the aerodynamic forces, thereby widening the wind speed range for energy harvesting.  
47 Wang *et al.* [30] introduced the metasurface concept in the design of a VIVPEH for  
48 the first time. The results demonstrated that by decorating the circular cylinder bluff  
49  
50  
51  
52  
53  
54  
55  
56  
57  
58  
59  
60  
61  
62  
63  
64  
65

1 body with a suitable metasurface, the synchronization region of the VIVPEH can be  
2 enlarged by 63.64%. Furthermore, the voltage output amplitude can also be  
3 remarkably increased.

4 Unlike VIVPEHs, galloping-based piezoelectric energy harvesters (GPEHs) are  
5 not restricted by lock-in region and can realize energy harvesting at higher wind  
6 speeds. Regarding the underlying mechanism of galloping, some fundamental studies  
7 can be found in the following literature. Den Hartog [31] provided an early  
8 explanation of the galloping vibration of a transmission line due to the action of a  
9 transverse wind. Scruton [32] employed statistical concepts to estimate dynamic  
10 responses caused by random fluctuations in atmospheric wind speed. Parkinson [33,  
11 34] developed an analytical model based on quasi-steady approximation and  
12 successfully predicted the galloping amplitude of a square-section bluff body. More  
13 extensive discussions on this subject can be found in the books [35, 36]. Recently, the  
14 research of GPEHs has attracted lots of interest. Barrero-Gil *et al.* [37] developed a  
15 lumped parameter model to describe and predict the dynamics of a GPEH. Sirohi *et al.*  
16 [38] theoretically and experimentally studied a GPEH with a D-shaped cross-section  
17 bluff body. The results showed that when the wind speed was 10.5 miles per hour, the  
18 maximum power produced by the GPEH could reach 1.14 mW. Abdelkefi *et al.* [39]  
19 designed a GPEH with a square-section bluff body and investigated the influence of  
20 Reynolds number on its cut-in wind speed and output power. The results revealed that  
21 load resistance and Reynolds number play a crucial role in affecting the output power.  
22 Wang *et al.* [40] used metasurfaces in designing the square-section bluff body of a  
23 GPEH. It was found that the maximum output voltage of the GPEH with a  
24 square-section bluff body wrapped on the convex cylindrical metasurface was  
25 increased by more than 20%.

26 Heat exchangers are the essential devices to realize heat transfer in refrigeration,  
27 air conditioning, power stations, chemical plants, etc. However, the ash deposition of  
28 dusty flue gas in the boiler and heat exchanger often threatens the safety of the  
29 equipment and affects the heat exchange performance. Therefore, a lot of research on  
30 the ash deposition phenomenon in heat exchangers has been carried out. Han *et al.* [41]  
31 studied the ash deposition on the surface of a tube-row heat exchanger. They also  
32 analyzed the influence of the particle size, the flow rate, and the tube bank shape on  
33 the ash deposition phenomenon. Bouris *et al.* [42] investigated the drop-shaped  
34 arrangement of tube bundles. The results indicated that while the heat transfer  
35 coefficient of the tube bundles was increased, the particle deposition rate and the  
36 pressure drop were reduced by 75% and 40%, respectively. Mavridou *et al.* [43]  
37 employed numerical methods to calculate the particle deposition and evaluate the heat  
38 transfer performance of circular tubes with various diameters. Compared to the  
39 standard configuration, the particle deposition rate decreased by 30%, and the heat  
40 transfer per unit volume increased by 28%. However, ash deposition in the flue might  
41 not always have a negative effect. The cross-section shape of the heat exchange tube  
42 will be changed as the ash deposition is formed. Considering the flow field  
43 environment in the flue gas tube, these factors have significant research value in  
44 FIV-based piezoelectric energy harvesting (FIVPEH). Therefore, this paper examines  
45  
46  
47  
48  
49  
50  
51  
52  
53  
54  
55  
56  
57  
58  
59  
60  
61  
62  
63  
64  
65

1 the ash deposition effect on FIVPEH for the first time. According to the cross-section  
2 shape of the heat exchanger tube under the effect of ash deposition, two new bluff  
3 body shapes, namely bell-shaped and horn-shaped, are designed. The ash deposition  
4 lengths are varied to simulate the variation of the pipe shape at different ash  
5 deposition times. Subsequently, the ash deposited FIVPEHs are comprehensively  
6 studied, including performance comparison, parameter analysis, and flow field  
7 analysis through wind tunnel experiments and CFD simulation.  
8  
9

## 10 **2. Design concepts and experiment setup**

### 11 **2.1 Design concepts**

12  
13  
14  
15  
16  
17  
18 During the combustion process, the high temperature in a furnace causes  
19 inorganic substances to undergo complex physical and chemical reactions, turning  
20 them into gases, liquids, and solids. All of them exist in the flue gas pipeline in the  
21 form of fly ash. Ash is formed due to the deposition of those inorganic materials in  
22 solid fuels after combustion [44]. When the flue gas flows through the heat exchanger,  
23 fly ash will deposit on the surface of the heat exchange tube. Because the fly ash in  
24 the flue gas pipe has a variety of physical states and the particle size of the ash  
25 particles ranges from nanometers to micrometers, there are several types of deposition  
26 mechanisms [45], including thermophoresis, inertial impaction, and eddy impaction.  
27 The ash deposition formed due to the first two mechanisms is usually located on the  
28 windward side of the tube. The ash deposition due to eddy impaction is often formed  
29 on the leeward side of the tube since the ash particles are too slight to separate from  
30 the flue gas flow and follow the airflow to the leeward side of the tube. Due to the  
31 eddy disturbance generated by the flow around the bluff body, the fly ash always  
32 deposits on the backside of the tube [46]. The schematic diagram of a general ash  
33 deposition process is shown in **Fig. 1**.  
34  
35  
36  
37  
38  
39  
40  
41  
42  
43  
44  
45  
46  
47  
48  
49  
50  
51  
52  
53  
54  
55  
56  
57  
58  
59  
60  
61  
62  
63  
64  
65

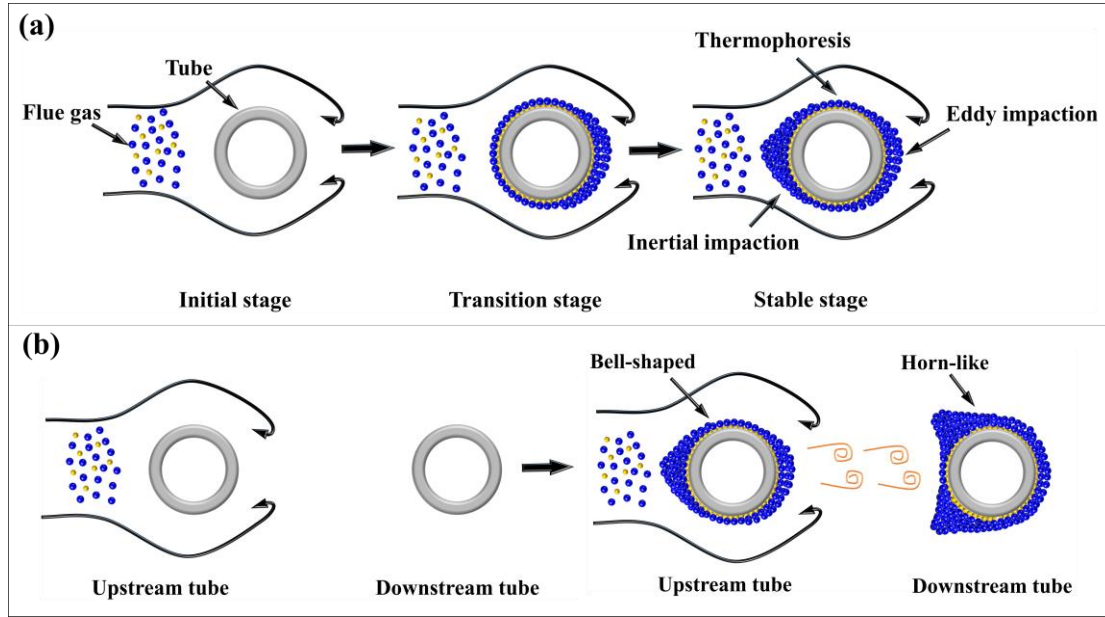


**Fig. 1.** (a) Schematic diagram of the three-stage process of ash deposition formation on a tube in heat exchange systems; (b) Schematic diagram of ash deposition shapes formed on multi-tubes in heat exchange systems.

Inspired by the deposition behavior of ash particles on the tube surface, this paper proposes to install a flow-induced piezoelectric energy harvester (FIVPEH) in the flue where aerokinetic energy exists. Ash deposition on the elliptic cylinder bluff body is considered, and its effect on the energy harvesting performance is investigated. Various shapes of ash depositions might lead to different aerodynamic characteristics of the bluff body. Therefore, two bluff bodies with differently shaped ash depositions are designed. **Fig. 2** exhibits the schematic diagram of the two FIVPEHs with different ash deposition attached to the bluff bodies. According to the geometric profile, the bluff bodies presented in **Fig. 2** (a) and (b) are referred to as bell-shaped and horn-like bluff bodies, respectively. According to the literature [44, 45], for a number tubes placed in series in the heat exchange system, the bell-shaped ash deposition is formed only on the first tube. Due to the influence of the wake of the upstream tube, horn-shaped ash depositions are formed on the remaining tubes. Both shapes of ash deposition are present in practice. In order to achieve a FIVPEH with a bell-shaped bluff body, one can install the FIVPEH in the front of all the tubes in the heat exchange system. To obtain a FIVPEH with a horn-shaped bluff body, one can install the FIVPEH at least after the first tube.

Each FIVPEH consists of a bluff body, a cantilever beam, and a piezoelectric transducer. The height of the bluff body is  $H$ . The length, width, and thickness of the cantilever beam are  $L$ ,  $W$ , and  $T_b$ , respectively. **Fig. 2** (c) shows the key parameters that determine the geometric profiles of the bell-shaped and horn-like bluff bodies. Each bluff body is composed of a principal elliptic cylinder and one/two segmented ellipses. The segmented ellipse is an imitation of the ash deposition. The major and minor axes of the principal ellipse are  $a_1$  and  $b_1$ , and  $a_1 \times b_1 = 30 \text{ mm} \times 20 \text{ mm}$ . The major and minor axes of the segmented ellipse are  $a_2$  and  $b_2$ , and  $a_2 \times b_2 = 24 \text{ mm} \times 10 \text{ mm}$ . For the bell-shaped bluff body, the major axes of the principal ellipse and the



segmented ellipse are on the same horizontal line. The distance between the left ends of the two ellipses is  $d_1$ . Considering that ash deposition may gradually grow, four bell-shaped bluff bodies with different ash deposition sizes are investigated by increasing  $d_1$  from 3 mm to 12 mm with a step of 3 mm. For the horn-like bluff body, the two segmented ellipses are installed symmetrically on the two sides of the major axis of the principal ellipse. The angle between the major axes  $a_1$  and  $a_2$  is  $45^\circ$ . The distance from the end of the segmented ellipse to the edge of the principal ellipse is  $d_2$ . Similarly, four different  $d_2$  (3 mm, 6 mm, 9 mm, and 12 mm) are selected to simulate the ash deposition growth.

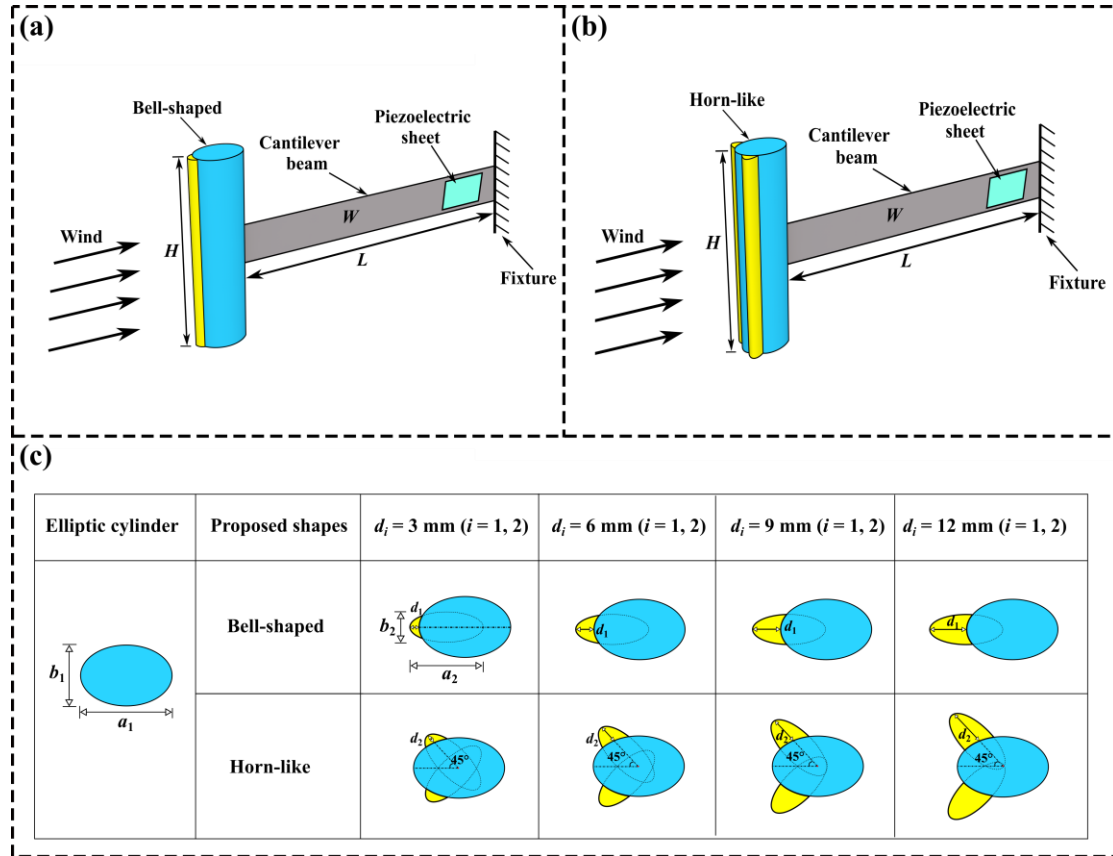


**Fig. 2.** Schematics of PEHs with different ash depositions: (a) bell-shaped ash deposition; (b) horn-like ash deposition; (c) geometries of the ash deposited bluff bodies.

## 2.2 Experimental setup

**Fig. 3** presents the experimental setup and the physical prototypes of the PEH with bell-shaped and horn-like bluff bodies. A PEH with an ordinary bluff body without ash deposition is used as the baseline model for comparison. In the experiment, the PEHs are, separately, placed in an open wind tunnel with a diameter of 400 mm. The turbulence intensity is controlled to be less than 1.0 %. The bluff body is made of rigid foam material. The major axis, the minor axis, and the height of the elliptic cylinder bluff body are 30 mm, 20 mm, and 118 mm, respectively. The cantilever beam is made of aluminum, and its dimensions are  $L \times W \times T_b = 184 \text{ mm} \times 25 \text{ mm} \times 0.5 \text{ mm}$ . The capacitance  $C_p$  of the piezoelectric transducer (PZT-5, Jiaye-shi

Co, China) is 24.87 nF. The wind speed in the wind tunnel is controlled by a draught fan and is measured by a hot-wire anemometer (405i, Testo Company, USA). The two-stage honeycomb device straightens the wind generated by the draught fan. The wind speed range investigated in this paper is from 0.87 m/s to 3.61 m/s. The natural frequencies of all the PEHs are calibrated to be almost the same, approximately 8.0 Hz. The displacements of the bluff bodies are measured by a laser displacement sensor (Panasonic: HG-C1400) with a resolution of 300  $\mu\text{m}$ . The signals are recorded using a dual-channel USB data acquisition instrument (USB DAQ-280G). The voltage generated by the piezoelectric transducer is recorded by a data acquisition apparatus (DS1104S, RIGOL, China).

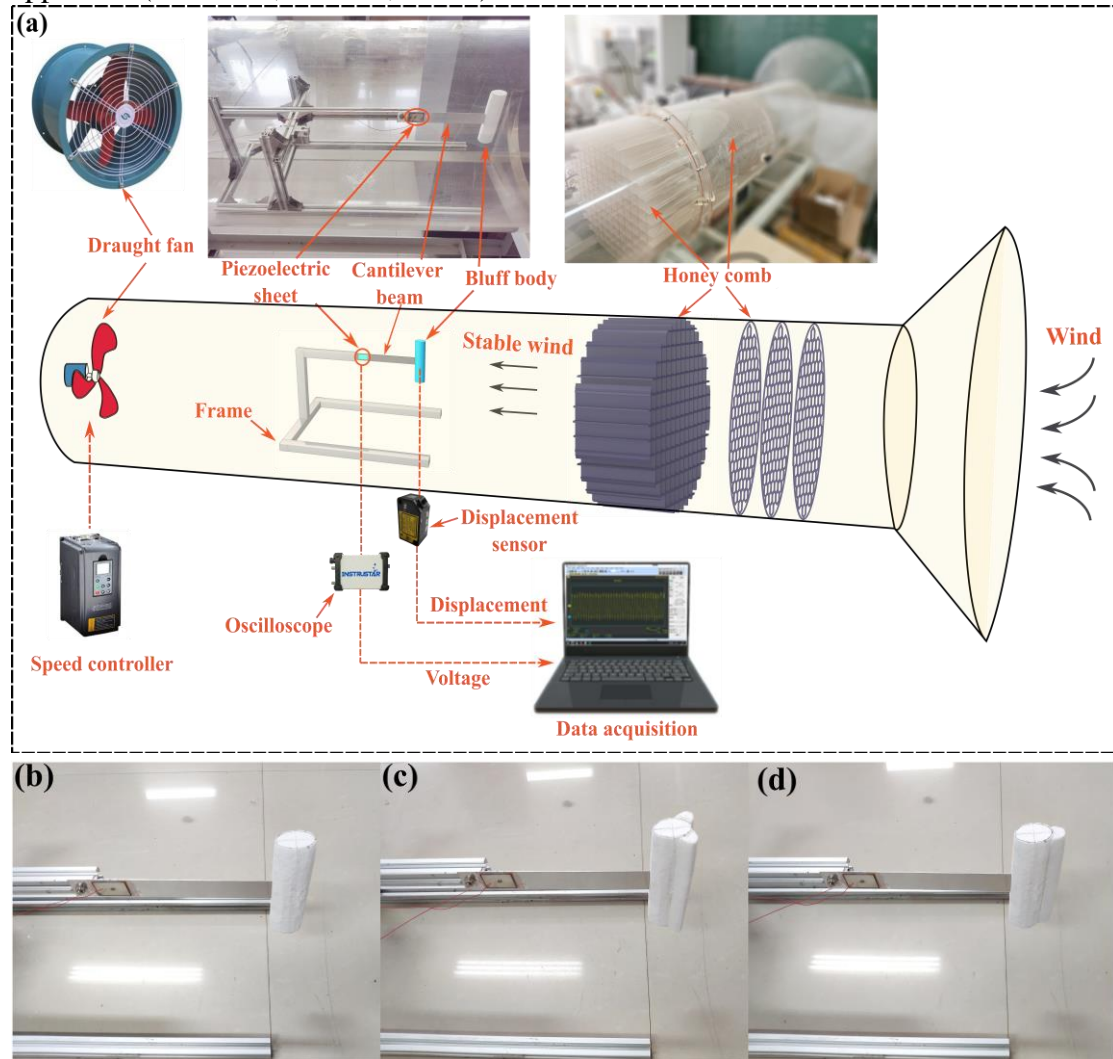


**Fig. 3.** (a) The experimental setup; (b) the fabricated baseline PEH; (c) the fabricated PEH with the horn-like bluff body; (d) the fabricated PEH with the bell-shaped bluff body.

### 3. Results and discussion

#### 3.1 The elliptic cylinder bluff body

The wind tunnel test results of the PEH with the elliptic cylinder bluff body are

illustrated in **Fig. 4** and **Fig. 5**. **Fig. 4** (a) and (b) present the output voltage and vibration amplitude responses, respectively. A lock-in region, with lower and upper bounds of 1.41 m/s and 2.51 m/s, is observed in the response diagram. It indicates that the PEH with the elliptic cylinder bluff body exhibits VIV. Over the lock-in region, with the increase of wind speed, the output voltage from the PEH first increases, then decreases. A maximum voltage of 2.33 V is obtained when the wind speed reaches 1.82 m/s. When the wind speed exceeds 2.51 m/s beyond the lock-in region, the voltage output becomes negligibly small. The displacement response of the PEH presented in **Fig. 4** (b) exhibits a similar behavior. Appreciable vibration of the PEH occurs only within the lock-in region. The vibration amplitude reaches a maximum value of 7.06 mm at the wind speed of 2.51 m/s.

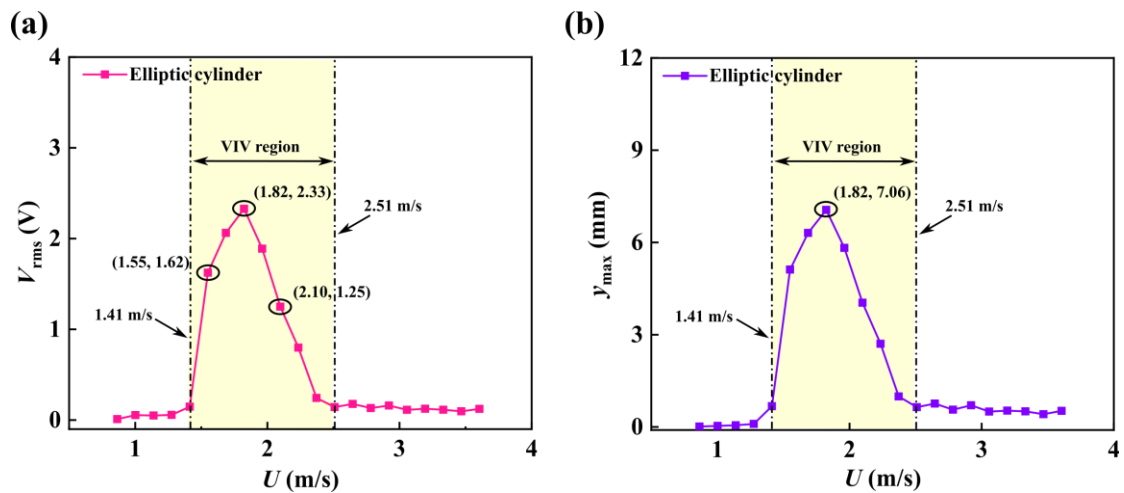


**Fig. 4.** Results of the PEH with elliptic cylinder bluff body: (a) RMS voltage output (b) maximum vibration displacement of the bluff body.

**Fig. 5** exhibits the dominant vibration frequency of the PEH in the VIV region, and the voltage time-history is plotted at the wind speeds of 1.55 m/s, 1.82 m/s, and 2.10 m/s. The three wind speeds are, respectively, taken from the initial excitation branch, upper branch, and lower branch of the VIV region. In **Fig. 5** (a), it is noted that the dimensionless frequency gradually increases to 1 as the wind speed increases, then keeps growing as the wind speed increases. However, the frequency shift in the lock-in region is minor, and the frequency ratio is always around 1. This phenomenon agrees with the results in the literature [47]. Thus, it further proves that the PEH with the elliptic cylinder bluff body performs VIV. It can be seen from **Fig. 5** (b) that at all the three wind speeds, the PEH undergoes harmonic vibration. Due to the locking phenomenon, the output voltage of the PEH at the wind speed of 1.82 m/s is obviously larger than that when the wind speed is changed to 1.55 m/s or 2.10 m/s.

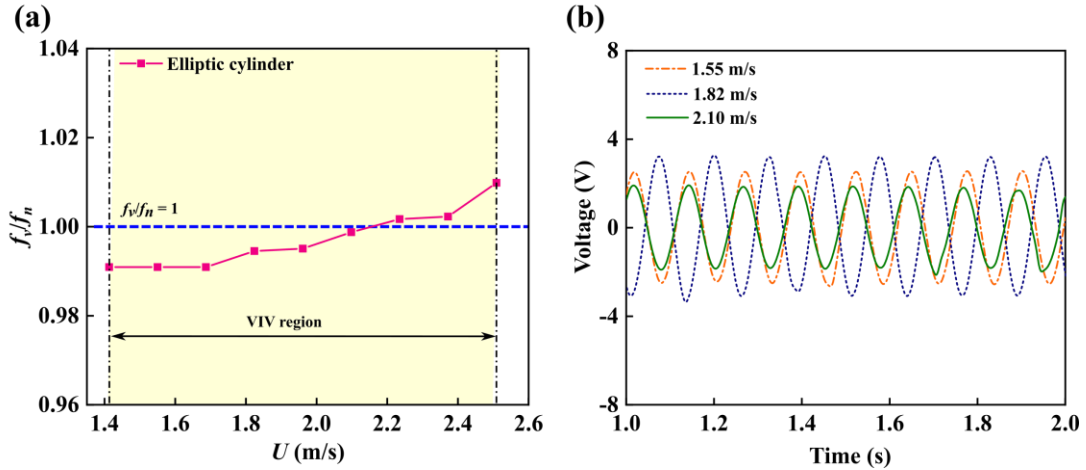


**Fig. 5.** (a) The dominant non-dimensional frequency of the PEH with elliptic cylinder bluff body under different wind speeds. (b) the voltage output time histories at the wind speeds 1.55 m/s, 1.82 m/s, and 2.10 m/s.

### 3.2 The Bell-shaped bluff body

As seen in **Fig. 6**, the bell-shaped additions produce a decrease in the amplitude of motion and a reduction of the voltage generated. For the PEH with the elliptic cylinder bluff body, the VIV phenomenon occurs over the wind speed range  $U = 1.41$  m/s  $\sim$  2.51 m/s. A maximum output voltage of 2.33 V is obtained at the wind speed of 1.82 m/s. For the PEH with the bell-shaped bluff body, for  $d_1$  equal to 3 mm, 6 mm, 9 mm, and 12 mm, the maximum voltage correspondingly becomes 0.99 V, 0.77 V, 0.44 V, and 0.49 V, and the maximum amplitude is 3.35 mm, 2.93 mm, 1.75 mm, and 1.79 mm, respectively. In other words, bell-shaped bluff bodies are not beneficial for energy harvesting. In contrast, they demonstrate the potential application for suppressing galloping-induced vibrations. Moreover, optimizing the parameters of the bell-shaped bluff body may lead to a maximum suppression performance. For instance, in the above case studies, the bell-shaped bluff body with  $d_1 = 9$  mm shows the strongest vibration suppression effect: its maximum amplitude is reduced by 75%, compared to the baseline model.

The time history responses of the PEH with the bell-shaped bluff body ( $d_1 = 9$  mm) at  $U = 1.41$  m/s are presented in **Fig. 6** (c) and (d). The results of the baseline model at  $U = 1.82$  m/s are also presented for comparison.  $U = 1.41$  m/s and 1.82 m/s are the optimal wind speeds to achieve the maximum voltage output for each case. Both cases exhibit harmonic vibration, while the baseline model has a significantly larger vibration amplitude, which is consistent with the results in **Fig. 6** (a) and (b).

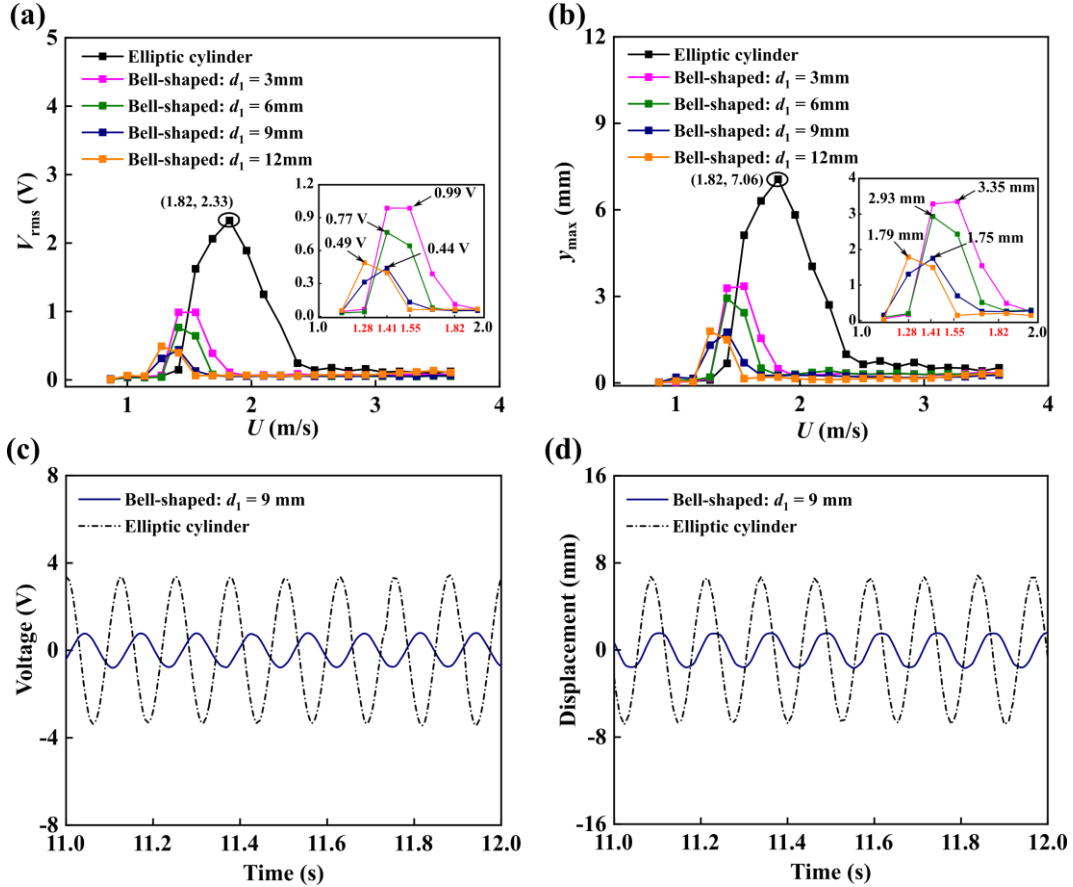


**Fig. 6.** Performance comparison of the PEHs with different bluff bodies: (a) RMS voltage outputs; (b) maximum vibration displacement of the bluff bodies; (c) time-history voltage output and (d) displacement of the PEHs with the bell-shaped bluff body under the optimal wind speed of  $U = 1.41$  m/s and the elliptic cylinder bluff body under the optimal wind speed of  $U = 1.82$  m/s.

### 3.3 The Horn-like bluff body

The results of the PEH with the horn-like bluff body of varying  $d_2$  are presented in **Fig. 7**. The results of the baseline model are also provided for comparison. **Fig. 7** (a) clearly shows that, unlike the baseline model, the PEH with the horn-like bluff body mainly exhibits the galloping phenomenon, regardless of the values of  $d_2$ . Hence, the PEH with the horn-like bluff body can produce significant voltage outputs over a much wider wind speed range. Moreover, unlike the behavior in the VIV region of the baseline model, with the increase of the wind speed, the voltage output monotonically increases. Over the wind speed range under investigation, for  $d_2$  equal to 3 mm, 6 mm, 9 mm, and 12 mm, the maximum voltage output of the PEH with the horn-like bluff body correspondingly becomes 14.06 V, 14.36 V, 14.20 V, and 14.24 V, which are much larger than that of the baseline model (2.33 V). **Fig. 7** (b) compares the displacement response of the PEH with the horn-like bluff body. For  $d_2$  equal to 3 mm, 6 mm, 9 mm, and 12 mm, the maximum displacement of the PEH with the horn-like bluff body becomes 49.96 mm, 56.32 mm, 54.45 mm, and 55.46 mm, which indicate 607%, 697%, 671%, and 685% increases compared to the baseline model. Among the

above cases, using the horn-like bluff body with  $d_2$  of 6 mm leads to the best performance. Its maximum voltage output is increased by 516% compared to the baseline model. In addition, the cut-in wind speed of the optimal design, i.e.,  $d_2 = 6$  mm, is about 1.28 m/s, which is smaller by 9% compared to the baseline model. Therefore, using the horn-like bluff body is also favorable for low wind speed energy harvesting.

In fact, the significant increase of the voltage output is the consequence of the galloping phenomenon. And the low cut-in wind speed advantage is inherited from the VIV behavior. In the enlarged views in **Fig. 7** (a) and (b), it is noted that over the wind range 1.1 m/s  $\sim$  1.8 m/s, when  $d_2 = 3$  mm or 6 mm, the PEH with the horn-like bluff body undergoes VIV: the voltage/displacement response first increases, then decreases. When  $d_2 = 9$  mm or 12 mm, the VIV phenomenon appears in the wind speed range of 1.28 m/s  $\sim$  1.69 m/s. The time-history responses of the optimal design ( $d_2 = 6$  mm) at  $U = 1.82$  m/s, which is the optimal wind speed of the baseline model, are presented in **Fig. 7** (c) and (d). It can be seen in **Fig. 7** (a) that both cases exhibit harmonic vibration. Even  $U = 1.82$  m/s is the optimal wind speed of the baseline model, while not for the PEH with the horn-like bluff body; the voltage and displacement responses of the PEH with the horn-like bluff body are still larger than those of the baseline model. In brief, the PEH with the horn-like bluff body demonstrates a superior wind energy harvesting ability.

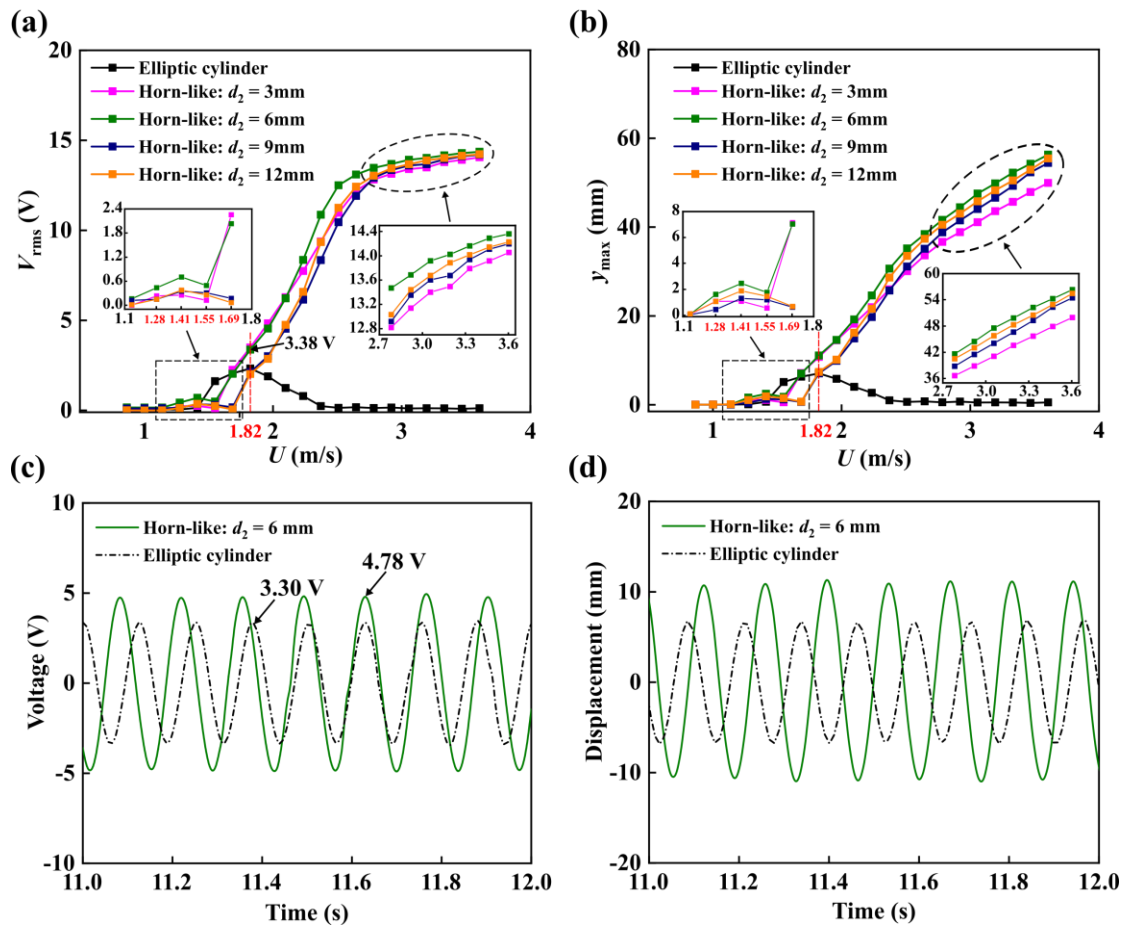


**Fig. 7.** Performance comparison of the PEHs with different bluff bodies: (a) RMS voltage outputs;

(b) maximum vibration displacement of the bluff bodies; (c) time-history voltage output and (d) displacement of the PEHs with the horn-like bluff body and the elliptic cylinder bluff body under the wind speed of  $U = 1.82$  m/s.

#### 4. Interpretation based on CFD simulation

Computational fluid dynamics (CFD) simulations are carried out to further reveal the effect of ash deposition on the aerodynamics of the bluff body. CFD models are built using the commercial software XFlow, which adopts the lattice Boltzmann method. The dimensions of the bluff bodies in simulations are consistent with those of the physical prototypes tested in the experiments. The calculation domain set in the simulation is a rectangle with a length of  $40b_1$  and a width of  $20b_1$ , where  $b_1$  is the length of the minor axis of the principal ellipse of the bluff body. The left and right boundary conditions of the calculation domain are set as velocity inlet and flow outlet, respectively. The fluid is air. The upper and lower boundary conditions are set to be walls. The distance between the center of the bluff body and the upper boundary is  $10b_1$ , and that to the outlet boundary is  $30b_1$  to ensure that the flow field behind the bluff body can be fully developed. In the CFD simulations, the external single-phase forced incompressible model is selected to simulate the flow. The time step is automatically fixed to  $5 \times 10^{-5}$  s. The Reynolds number of the simulated flow field is approximately 2460.

As known from the results presented in the previous section, using the bell-shaped bluff body leads to vibration suppression and a deteriorated energy harvesting performance. On the contrary, using the horn-like bluff body induces the galloping phenomenon and significantly improves the energy harvesting performance. **Fig. 8** presents the vorticity contours of the bell-shaped ( $d_1 = 9$  mm), elliptic cylinder, and horn-like ( $d_2 = 6$  mm) bluff bodies at different time stages to reveal the aerodynamic mechanisms behind the above conclusion. From **Fig. 8**, one can find that for the bell-shaped bluff body, the presence of a small elliptical bulge in the front streamlines the oncoming flow over the bluff body. Thus, the vortex shedding is similar to that of the elliptic cylinder bluff body: in both cases, primary large-scale vortices (PV) are produced behind the bluff bodies. The width of the wake is evaluated to indicate the intensity of the vortex shedding. The widths of the wake produced after the bell-shaped and elliptic cylinder bluff bodies are  $1.57b_1$  and  $1.79 b_1$ , respectively. This implies that the intensity of the vortex shedding of the bell-shaped bluff body is weaker than that of the elliptic cylinder. This explains why the vibration amplitude of the bell-shaped bluff body is smaller than that of the elliptic cylinder one. Unlike the elliptic cylinder bluff body, for the horn-like one, due to the presence of two small elliptical bulges, not only primary large-scale vortices (PV), but also small-scale secondary vortices (SV) are produced in the wake flow. Because of the interaction between PV and SV, the vortex shedding effect is delayed, resulting in a significant increase of the wake vortices. Moreover, it is observed that the wake width of the horn-like bluff body is much wider than that of the elliptic cylinder one, which indicates a stronger aerodynamic instability in the wake. Therefore, unlike the

vibration mode of the elliptic cylinder bluff body, the vibration mode of the horn-like bluff body is galloping, which can induce a larger-amplitude vibration and produce a higher voltage output. In summary, the formation of small-scale secondary vortices (SV) plays a key role in the intensity of vibration.

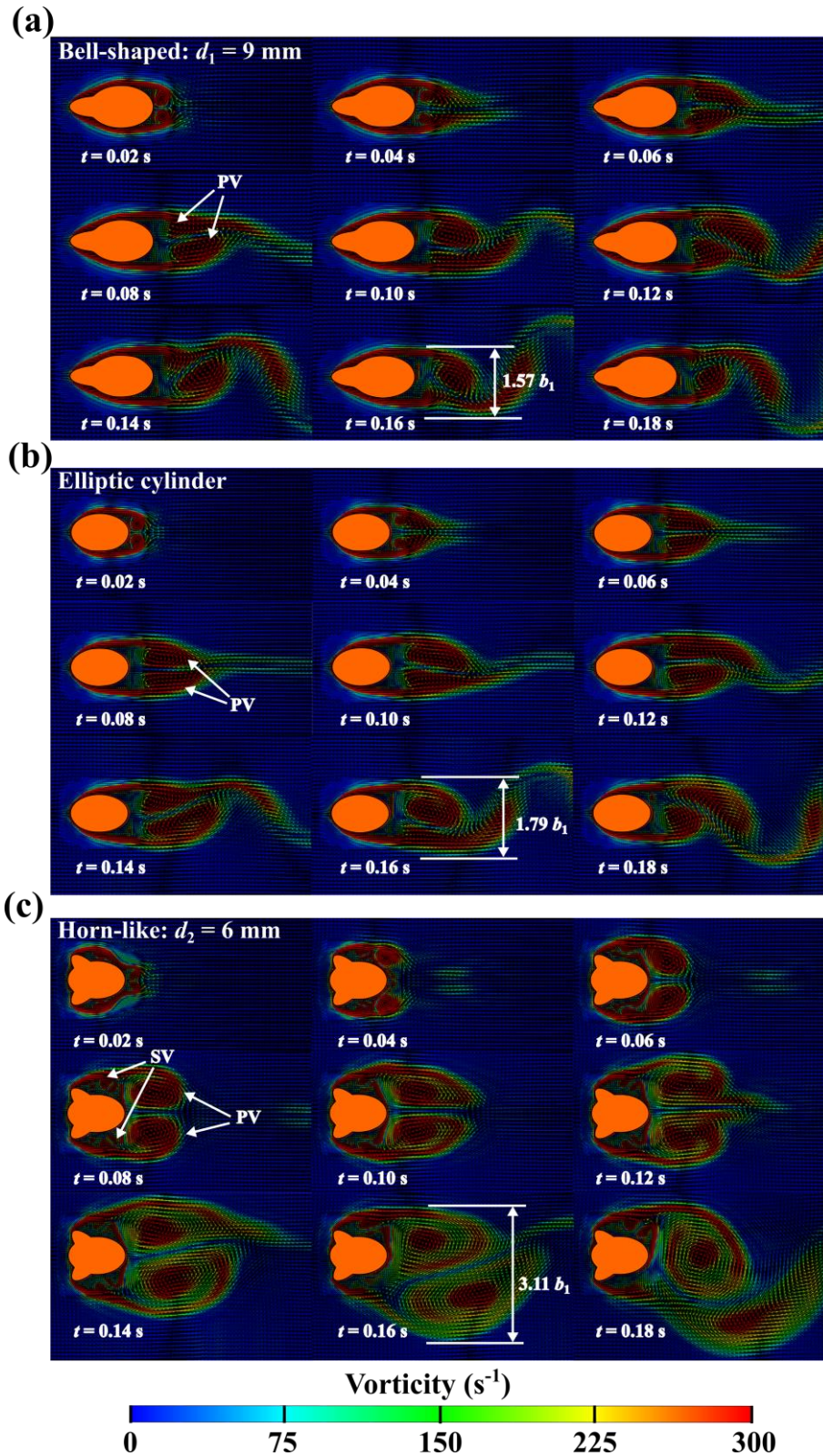
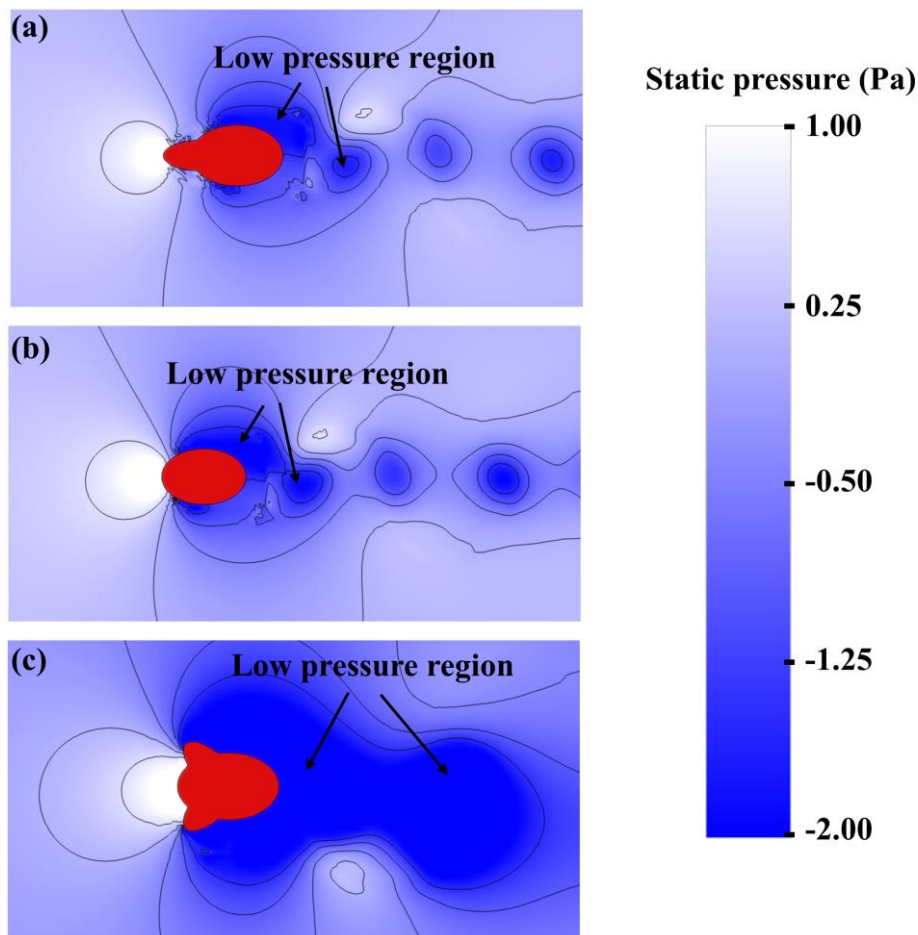


Fig. 8. Comparison of flow-field evolution with time for the three bluff bodies at the wind speed



of  $U = 1.82$  m/s: (a) the bell-shaped ( $d_1 = 9$  mm) bluff body; (b) the elliptic cylinder bluff body; (c) the horn-like ( $d_2 = 6$  mm) bluff body.

The pressure contours around the bell-shaped ( $d_1 = 9$  mm), elliptic cylinder, and horn-like ( $d_2 = 6$  mm) bluff bodies at the wind speed of 1.82 m/s are shown in **Fig. 9**. Obviously, it can be observed that the low-pressure region around the horn-like bluff body is significantly larger than those around the other two bluff bodies. The larger pressure difference causes the horn-like bluff body to vibrate more violently than the other two bluff bodies. Comparing the bell-shaped and elliptic cylinder bluff bodies, the low-pressure region around the bell-shaped bluff body is smaller than that around the elliptic cylinder bluff body. Therefore, the bell-shaped bluff body undergoes the smallest vibration. **Fig. 10** presents the velocity contours of the bell-shaped ( $d_1 = 9$  mm), elliptic cylinder, and horn-like ( $d_2 = 6$  mm) bluff bodies at the wind speed of 1.82 m/s. The high-velocity region in **Fig. 10** corresponds to the low-pressure region in **Fig. 9**. The high-velocity region around the horn-like bluff body is the largest, which enhances the oscillation of the horn-like bluff body, and makes its vibration significantly higher than the other two bluff bodies. The above discussion agrees well with the conclusions obtained from the experiments in the previous section.



**Fig. 9.** Pressure contour around (a) the bell-shaped ( $d_1 = 9$  mm) bluff body; (b) the elliptic cylinder bluff body; (c) the horn-like ( $d_2 = 6$  mm) bluff body at the wind speed of 1.82 m/s.

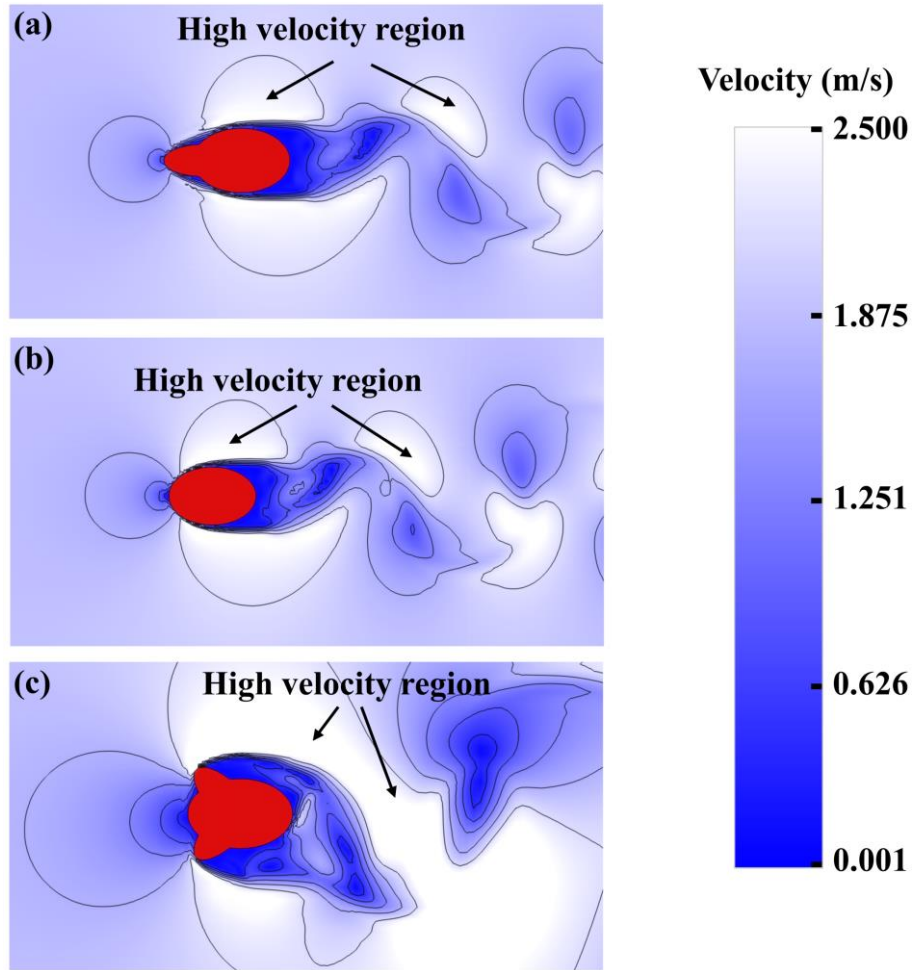


**Fig. 10.** Velocity contour around (a) the bell-shaped ( $d_1 = 9$  mm) bluff body; (b) the elliptic cylinder bluff body; (c) the horn-like ( $d_2 = 6$  mm) bluff body at the wind speed of 1.82 m/s.

## 5. Conclusion

This paper has explored the effect of ash deposition on flow-induced vibration energy harvesting in heat exchange systems. According to the shape and size of ash deposition, bell-shaped and horn-like bluff bodies have been proposed to simulate different ash depositions. Experimental results have revealed that the bell-shaped bluff bodies can suppress vibrations and are not beneficial for energy harvesting. In contrast, the horn-like bluff bodies can improve the energy harvesting performance by transforming VIV to galloping. The combination of VIV and galloping reduces the cut-in wind speed of the PEH and increases the voltage outputs under high wind speeds. The voltage output of an optimal prototype with  $d_2 = 6$  mm has been increased by 516%. Besides, CFD simulations have been conducted to interpret the underlying mechanisms behind the phenomena. For the bell-shaped bluff body, a weaker aerodynamic force is generated because the wake width is smaller than that of the elliptic cylinder bluff body. Thus, the vibration of the bluff body is diminished. For the horn-like bluff body, due to the interaction of PV and SV, the wake width is increased, resulting in an increased aerodynamic force. The flow-induced vibration

1 transforms from VIV to galloping. Therefore, a larger voltage output is generated by  
2 the PEH with the horn-like bluff body. In summary, a potential usefulness of the  
3 harmful ash deposition phenomenon in the flue gas pipeline for benefiting energy  
4 harvesting has been proposed and explored. Different ash deposition effects have been  
5 investigated. The work presented in this paper represents a preliminary study of the  
6 ash deposition effect on flow-induced vibration energy harvesting.  
7  
8  
9

## 10 **Acknowledgments**

11  
12 This work was supported by the National Natural Science Foundation of China  
13 (Grant No. 51977196), the China Postdoctoral Science Foundation (Grant No.  
14 2020T130557), the Natural Science Foundation of Excellent Youth of Henan Province  
15 (Grant No. 222300420076), and the State Key Laboratory of Structural Analysis for  
16 Industrial Equipment, Dalian University of Technology, China (GZ21114).  
17  
18  
19  
20

## 21 **References**

- 22  
23  
24 [1] J. Wang, L. Geng, L. Ding, H. Zhu, D. Yurchenko, The state-of-the-art review on energy harvesting  
25 from flow-induced vibrations, *Appl. Energy*, 267 (2020) 114902.  
26  
27 [2] X.W. Fu, Y.S. Yang, Modeling and analysis of cascading node-link failures in multi-sink wireless  
28 sensor networks, *Reliab. Eng. Syst. Saf.*, 197 (2020) 15.  
29  
30 [3] Z. Lai, S. Wang, L. Zhu, G. Zhang, J. Wang, K. Yang, D. Yurchenko, A hybrid piezo-dielectric wind  
31 energy harvester for high-performance vortex-induced vibration energy harvesting, *Mech. Syst. Signal*.  
32 *Process.*, 150 (2021).  
33  
34 [4] C. Magazzino, M. Mele, N. Schneider, A machine learning approach on the relationship among  
35 solar and wind energy production, coal consumption, GDP, and CO2 emissions, *Renew. Energ.*, 167  
36 (2021) 99-115.  
37  
38 [5] J.J. Yoo, G. Seo, M.R. Chua, T.G. Park, Y.L. Lu, F. Rotermund, Y.K. Kim, C.S. Moon, N.J. Jeon, J.P.  
39 Correa-Baena, V. Bulovic, S.S. Shin, M.G. Bawendi, J. Seo, Efficient perovskite solar cells via  
40 improved carrier management, *Nature*, 590 (2021) 10.  
41  
42 [6] C.H. Li, S.C. Xu, J. Yu, Z. Li, W.F. Li, J.H. Wang, A.H. Liu, B.Y. Man, S.K. Yang, C. Zhang, Local  
43 hot charge density regulation: Vibration-free pyroelectric nanogenerator for effectively enhancing  
44 catalysis and in-situ surface enhanced Raman scattering monitoring, *Nano Energy*, 81 (2021) 10.  
45  
46 [7] J.L. Wang, S.H. Gu, C.Y. Zhang, G.B. Hu, G. Chen, K. Yang, H. Li, Y.Y. Lai, G. Litak, D.  
47 Yurchenko, Hybrid wind energy scavenging by coupling vortex-induced vibrations and galloping,  
48 *Energy Convers. Manag.*, 213 (2020) 11.  
49  
50 [8] T. Morbiato, C. Borri, R. Vitaliani, Wind energy harvesting from transport systems: A resource  
51 estimation assessment, *Appl. Energy*, 133 (2014) 152-168.  
52  
53 [9] M.A. Mustapa, O.B. Yaakob, Y.M. Ahmed, C.K. Rheem, K.K. Koh, F.A. Adnan, Wave energy  
54 device and breakwater integration: A review, *Renew. Sust. Energ. Rev.*, 77 (2017) 43-58.  
55  
56 [10] C. Chen, Z.Y. Liu, S.H. Wan, J.T. Luan, Q.Q. Pei, Traffic Flow Prediction Based on Deep  
57 Learning in Internet of Vehicles, *IEEE Trans. Intell. Transp. Syst.*, 22 (2021) 3776-3789.  
58  
59 [11] H.S. Kim, J.-H. Kim, J. Kim, A review of piezoelectric energy harvesting based on vibration,  
60 *International Journal of Precision Engineering and Manufacturing*, 12 (2011) 1129-1141.  
61  
62  
63  
64  
65

- 1 [12] F.K. Shaikh, S. Zeadally, Energy harvesting in wireless sensor networks: A comprehensive review,  
2 *Renew. Sust. Energ. Rev.*, 55 (2016) 1041-1054.
- 3 [13] S. Fang, X. Fu, X. Du, W.-H. Liao, A music-box-like extended rotational plucking energy  
4 harvester with multiple piezoelectric cantilevers, *Applied Physics Letters*, 114 (2019).
- 5 [14] X. Zhao, J. Cai, Y. Guo, C. Li, J. Wang, H. Zheng, Modeling and experimental investigation of an  
6 AA-sized electromagnetic generator for harvesting energy from human motion, *Smart. Mater. Struct.*,  
7 27 (2018).
- 8 [15] K. Fan, Y. Zhang, S. E. L. Tang, H. Qu, A string-driven rotor for efficient energy harvesting from  
9 ultra-low frequency excitations, *Appl. Phys. Lett.*, 115 (2019).
- 10 [16] Z. Yang, L. Tang, L. Yu, K. Tao, K. Aw, Modelling and analysis of an out-of-plane electret-based  
11 vibration energy harvester with AC and DC circuits, *Mech. Syst. Signal. Process.*, 140 (2020).
- 12 [17] G. Hu, C. Zhao, Y. Yang, X. Li, J. Liang, Triboelectric energy harvesting using an origami-inspired  
13 structure, *Appl. Energy*, 306 (2022) 118037.
- 14 [18] J. Wang, S. Zhou, Z. Zhang, D. Yurchenko, High-performance piezoelectric wind energy harvester  
15 with Y-shaped attachments, *Energy Conversion and Management*, 181 (2019) 645-652.
- 16 [19] A. Abdelkefi, Aeroelastic energy harvesting: A review, *International Journal of Engineering  
17 Science*, 100 (2016) 112-135.
- 18 [20] L.B. Zhang, H.L. Dai, A. Abdelkefi, L. Wang, Improving the performance of aeroelastic energy  
19 harvesters by an interference cylinder, *Appl. Phys. Lett.*, 111 (2017).
- 20 [21] K. Yang, T. Qiu, J. Wang, L. Tang, Magnet-induced monostable nonlinearity for improving the  
21 VIV-galloping-coupled wind energy harvesting using combined cross-sectioned bluff body, *Smart  
22 Materials and Structures*, 29 (2020).
- 23 [22] K. Yang, J.L. Wang, D. Yurchenko, A double-beam piezo-magneto-elastic wind energy harvester  
24 for improving the galloping-based energy harvesting, *Appl. Phys. Lett.*, 115 (2019) 5.
- 25 [23] A. Abdelkefi, A.H. Nayfeh, M.R. Hajj, Modeling and analysis of piezoaeroelastic energy  
26 harvesters, *Nonlinear Dyn.*, 67 (2011) 925-939.
- 27 [24] M. Bryant, E. Garcia, Modeling and Testing of a Novel Aeroelastic Flutter Energy Harvester,  
28 *Journal of Vibration and Acoustics-Transactions of the Asme*, 133 (2011) 011010.
- 29 [25] H. Wang, W. Yang, K.D. Nguyen, G. Yu, Wake-induced vibrations of an elastically mounted  
30 cylinder located downstream of a stationary larger cylinder at low Reynolds numbers, *Journal of Fluids  
31 and Structures*, 50 (2014) 479-496.
- 32 [26] H.D. Akaydin, N. Elvin, Y. Andreopoulos, The performance of a self-excited fluidic energy  
33 harvester, *Smart. Mater. Struct.*, 21 (2012).
- 34 [27] H.L. Dai, A. Abdelkefi, L. Wang, Theoretical modeling and nonlinear analysis of piezoelectric  
35 energy harvesting from vortex-induced vibrations, *J. Intell. Mater. Syst. Struct.*, 25 (2014) 1861-1874.
- 36 [28] V. Azadeh-Ranjbar, N. Elvin, Y. Andreopoulos, Vortex-induced vibration of finite-length circular  
37 cylinders with spanwise free-ends: Broadening the lock-in envelope, *Physics of Fluids*, 30 (2018).
- 38 [29] G. Hu, K.T. Tse, M. Wei, R. Naseer, A. Abdelkefi, K.C.S. Kwok, Experimental investigation on  
39 the efficiency of circular cylinder-based wind energy harvester with different rod-shaped attachments,  
40 *Appl. Energy*, 226 (2018) 682-689.
- 41 [30] J.L. Wang, S.K. Sun, L.H. Tang, G.B. Hu, J.R. Liang, On the use of metasurface for  
42 Vortex-Induced vibration suppression or energy harvesting, *Energy Convers. Manag.*, 235 (2021) 14.
- 43 [31] J.P.D. Hartog, Transmission line vibration due to sleet, *Transactions of the American Institute of  
44 Electrical Engineers*, 51 (1932) 1074-1076.
- 45  
46  
47  
48  
49  
50  
51  
52  
53  
54  
55  
56  
57  
58  
59  
60  
61  
62  
63  
64  
65

- 1 [32] C. Scruton, Wind effects on structures, James Clayton Lecture, Proceedings Institution of  
2 Mechanical Engineers, 185 (1971) 301-317.
- 3 [33] G.V. Parkinson, Wind-induced instability of structures, Philosophical Transactions of the Royal  
4 Society of London, A269 (1971) 395-409.
- 5 [34] G.V. Parkinson, Phenomena and modelling of flow-induced vibrations of bluff bodies, Progress in  
6 Aerospace Sciences, 26 (1989) 169-224.
- 7 [35] R.D. Blevins, Flow-Induced Vibration, Van Nostrand Reinhold, New York, 1990.
- 8 [36] M.P. Paidoussis, S.J. Price, E. De Langre, Fluid-structure interactions: cross-flow-induced  
9 instabilities, Cambridge University Press, 2010.
- 10 [37] A. Barrero-Gil, G. Alonso, A. Sanz-Andres, Energy harvesting from transverse galloping, J. Sound  
11 Vibr., 329 (2010) 2873-2883.
- 12 [38] J. Sirohi, R. Mahadik, Harvesting Wind Energy Using a Galloping Piezoelectric Beam, Journal of  
13 Vibration and Acoustics-Transactions of the Asme, 134 (2012).
- 14 [39] A. Abdelkefi, M.R. Hajj, A.H. Nayfeh, Power harvesting from transverse galloping of square  
15 cylinder, Nonlinear Dynamics, 70 (2012) 1355-1363.
- 16 [40] J. Wang, S. Sun, G. Hu, Y. Yang, L. Tang, P. Li, G. Zhang, Exploring the potential benefits of  
17 using metasurface for galloping energy harvesting, Energy Convers. Manag., 243 (2021).
- 18 [41] H. Han, Y.-L. He, W.-Q. Tao, Y.-S. Li, A parameter study of tube bundle heat exchangers for  
19 fouling rate reduction, International Journal of Heat and Mass Transfer, 72 (2014) 210-221.
- 20 [42] D. Bouris, E. Konstantinidis, S. Balabani, D. Castiglia, G. Bergeles, Design of a novel, intensified  
21 heat exchanger for reduced fouling rates, International Journal of Heat and Mass Transfer, 48 (2005)  
22 3817-3832.
- 23 [43] S.G. Mavridou, D.G. Bouris, Numerical evaluation of a heat exchanger with inline tubes of  
24 different size for reduced fouling rates, International Journal of Heat and Mass Transfer, 55 (2012)  
25 5185-5195.
- 26 [44] S.-Z. Tang, Y.-L. He, F.-L. Wang, Y.-B. Tao, Parametric study on fouling mechanism and heat  
27 transfer characteristics of tube bundle heat exchangers for reducing fouling considering the deposition  
28 and removal mechanisms, Fuel, 211 (2018) 301-311.
- 29 [45] Y. Cai, K. Tay, Z. Zheng, W. Yang, H. Wang, G. Zeng, Z. Li, S. Keng Boon, P. Subbaiah, Modeling  
30 of ash formation and deposition processes in coal and biomass fired boilers: A comprehensive review,  
31 Appl. Energy, 230 (2018) 1447-1544.
- 32 [46] S.-Z. Tang, M.-J. Li, F.-L. Wang, Z.-B. Liu, Fouling and thermal-hydraulic characteristics of  
33 aligned elliptical tube and honeycomb circular tube in flue gas heat exchangers, Fuel, 251 (2019)  
34 316-327.
- 35 [47] Navrose, S. Mittal, Lock-in in vortex-induced vibration, Journal of Fluid Mechanics, 794 (2016)  
36 565-594.
- 37  
38  
39  
40  
41  
42  
43  
44  
45  
46  
47  
48  
49  
50  
51  
52  
53  
54  
55  
56  
57  
58  
59  
60  
61  
62  
63  
64  
65

# On the Investigation of Ash Deposition Effect on Flow-Induced Vibration Energy Harvesting

Junlei Wang<sup>1</sup>, Shanghao Gu<sup>1</sup>, Daniil Yurchenko<sup>2</sup>, Guobiao Hu<sup>3,4\*</sup>, Ronghan Wei<sup>5,6</sup>

<sup>1</sup> School of Mechanical and Power Engineering, Zhengzhou University, Zhengzhou 450000, China

<sup>2</sup> Institute of Sound and Vibration Research, University of Southampton, Southampton, SO17 1BJ, UK.

<sup>3</sup> School of Civil and Environmental Engineering, Nanyang Technological University, 50 Nanyang Avenue, 639798, Singapore

<sup>4</sup> State Key Laboratory of Structural Analysis for Industrial Equipment, Dalian University of Technology, Dalian 116024, China

<sup>5</sup> School of Mechanics and Safety Engineering, Zhengzhou University, Zhengzhou 450000, China

<sup>6</sup> China Institute of Intelligent Sensing, Zhengzhou University, Zhengzhou 450000, China

\*Corresponding author: [guobiao.hu@ntu.edu.sg](mailto:guobiao.hu@ntu.edu.sg)

## Abstract

This paper proposes **harnessing** the aerokinetic energy in flue systems and it explores the effect of the ash deposition on flow-induced vibration energy harvesting performance. Bell-shaped and horn-like bluff bodies are designed to simulate different ash depositions on a conventional elliptic cylinder bluff body. Wind tunnel experiments **were** conducted to investigate the energy harvesting performance using different ash deposition distributed over the bluff bodies. The experimental results show that compared to the baseline model **of** a conventional elliptic cylinder bluff body, the bell-shaped bluff body suppresses the flow-induced vibration and deteriorates the energy harvesting performance. In contrast, the horn-like bluff body can benefit energy harvesting by reducing the **galloping** cut-in wind speed and increasing the voltage output. The voltage output of an optimal prototype using the horn-like bluff body is increased by 516%. Computational fluid dynamics (CFD) simulations **were** carried out to unveil the physical mechanisms behind the phenomena. The CFD analysis results indicate that the appearance of the small-scale secondary vortices (SV) widens the wake flow and increases the aerodynamic force produced by the horn-like bluff body. The flow-induced vibration of the harvester using the horn-like bluff body transforms from VIV to galloping. Therefore, it has been preliminarily demonstrated that the unfavorable ash deposition phenomenon in flue systems has the potential for promoting flow-induced vibration energy **harvesting**.

1 **Keywords:** ash deposition, energy harvesting, flow-induced vibration, galloping  
2  
3 vortex-induced vibration  
4

## 5 **1. Introduction**

6

7  
8 In recent years, low-power consumption devices have been massively used in  
9 various fields to develop the Internet of Things (IoTs) [1, 2]. Most of these devices are  
10 powered by traditional chemical batteries. However, they often have limited storage  
11 capacities but bulky volumes. In some particular scenarios, such as remote areas,  
12 underwater environments, implant health monitoring, batteries are difficult to replace  
13 and maintain [3]. Therefore, harvesting energy from the ambient environment to  
14 provide the necessary power supply becomes a suitable battery-free solution to  
15 address the above issue. Common natural sources that are widely accessible in our  
16 ambient environment include solar energy [4, 5], vibration energy [6], wind energy [7,  
17 8], and wave energy [9, 10]. Vibration energy harvesting refers to the technique of  
18 converting vibration energy into electrical energy through piezoelectric [11-13],  
19 electromagnetic [14, 15], or electrostatic [16, 17] transduction mechanisms. Due to  
20 the advantages of high power density, simple structure, and long service life,  
21 piezoelectric energy harvesting has attracted lots of research interest [18, 19].  
22

23  
24 Flow-induced vibration (FIV) is a natural phenomenon that ubiquitously exists in  
25 our ambient environment. Therefore, FIV-based energy harvesting technology has  
26 been extensively developed in recent years [20]. FIV phenomena can be further  
27 classified into vortex-induced vibration (VIV) [21], galloping [22], flutter [23, 24],  
28 and wake galloping [25]. VIV-based piezoelectric energy harvesters (VIVPEH) can  
29 efficiently generate considerable power in the lock-in region. However, when the flow  
30 velocity exceeds the lock-in region, the structural vibration will decrease significantly,  
31 and the energy harvesting performance will deteriorate dramatically. Researchers have  
32 devoted numerous efforts to improving the performance of VIVPEH. Akaydin *et al.*  
33 [26] designed a VIVPEH by connecting a cantilever beam to a cylindrical bluff body.  
34 The wind tunnel test showed that the designed VIVPEH could generate approximately  
35 a power of 0.1 mW at a wind speed of 1.192 m/s. Dai *et al.* [27] established a  
36 nonlinear distributed-parameter model for a VIVPEH. They discussed the influences  
37 of the bluff body, the piezoelectric sheet length, and the electrical resistance on the  
38 synchronization region and the performance of the harvester. Azadeh-Ranjba *et al.* [28]  
39 investigated the influence of the aspect ratio of the rigid cylinder on a VIVPEH. The  
40 results indicated that an appropriate aspect ratio could not only increase the power  
41 output of the VIVPEH but also broaden its lock-in region. In recent years, researchers  
42 have been showing interest in optimizing the surface structure of the bluff body to  
43 widen the lock-in region of a VIVPEH for broadband energy harvesting. For example,  
44 Hu *et al.* [29] added two rods to a circular cylinder bluff body of a VIVPEH to alter  
45 the aerodynamic forces, thereby widening the wind speed range for energy harvesting.  
46 Wang *et al.* [30] introduced the metasurface concept in the design of a VIVPEH for  
47 the first time. The results demonstrated that by decorating the circular cylinder bluff  
48  
49  
50  
51  
52  
53  
54  
55  
56  
57  
58  
59  
60  
61  
62  
63  
64  
65

1 body with a suitable metasurface, the synchronization region of the VIVPEH can be  
2 enlarged by 63.64%. Furthermore, the voltage output amplitude can also be  
3 remarkably increased.

4 Unlike VIVPEHs, galloping-based piezoelectric energy harvesters (GPEHs) are  
5 not restricted by lock-in region and can realize energy harvesting at higher wind  
6 speeds. Regarding the underlying mechanism of galloping, some fundamental studies  
7 can be found in the following literature. Den Hartog [31] provided an early  
8 explanation of the galloping vibration of a transmission line due to the action of a  
9 transverse wind. Scruton [32] employed statistical concepts to estimate dynamic  
10 responses caused by random fluctuations in atmospheric wind speed. Parkinson [33,  
11 34] developed an analytical model based on quasi-steady approximation and  
12 successfully predicted the galloping amplitude of a square-section bluff body. More  
13 extensive discussions on this subject can be found in the books [35, 36]. Recently, the  
14 research of GPEHs has attracted lots of interest. Barrero-Gil *et al.* [37] developed a  
15 lumped parameter model to describe and predict the dynamics of a GPEH. Sirohi *et al.*  
16 [38] theoretically and experimentally studied a GPEH with a D-shaped cross-section  
17 bluff body. The results showed that when the wind speed was 10.5 miles per hour, the  
18 maximum power produced by the GPEH could reach 1.14 mW. Abdelkefi *et al.* [39]  
19 designed a GPEH with a square-section bluff body and investigated the influence of  
20 Reynolds number on its cut-in wind speed and output power. The results revealed that  
21 load resistance and Reynolds number play a crucial role in affecting the output power.  
22 Wang *et al.* [40] used metasurfaces in designing the square-section bluff body of a  
23 GPEH. It was found that the maximum output voltage of the GPEH with a  
24 square-section bluff body wrapped on the convex cylindrical metasurface was  
25 increased by more than 20%.

26 Heat exchangers are the essential devices to realize heat transfer in refrigeration,  
27 air conditioning, power stations, chemical plants, etc. However, the ash deposition of  
28 dusty flue gas in the boiler and heat exchanger often threatens the safety of the  
29 equipment and affects the heat exchange performance. Therefore, a lot of research on  
30 the ash deposition phenomenon in heat exchangers has been carried out. Han *et al.* [41]  
31 studied the ash deposition on the surface of a tube-row heat exchanger. They also  
32 analyzed the influence of the particle size, the flow rate, and the tube bank shape on  
33 the ash deposition phenomenon. Bouris *et al.* [42] investigated the drop-shaped  
34 arrangement of tube bundles. The results indicated that while the heat transfer  
35 coefficient of the tube bundles was increased, the particle deposition rate and the  
36 pressure drop were reduced by 75% and 40%, respectively. Mavridou *et al.* [43]  
37 employed numerical methods to calculate the particle deposition and evaluate the heat  
38 transfer performance of circular tubes with various diameters. Compared to the  
39 standard configuration, the particle deposition rate decreased by 30%, and the heat  
40 transfer per unit volume increased by 28%. However, ash deposition in the flue might  
41 not always have a negative effect. The cross-section shape of the heat exchange tube  
42 will be changed as the ash deposition is formed. Considering the flow field  
43 environment in the flue gas tube, these factors have significant research value in  
44 FIV-based piezoelectric energy harvesting (FIVPEH). Therefore, this paper examines  
45  
46  
47  
48  
49  
50  
51  
52  
53  
54  
55  
56  
57  
58  
59  
60  
61  
62  
63  
64  
65



1 the ash deposition effect on FIVPEH for the first time. According to the cross-section  
2 shape of the heat exchanger tube under the effect of ash deposition, two new bluff  
3 body shapes, namely bell-shaped and horn-shaped, are designed. The ash deposition  
4 lengths are varied to simulate the variation of the pipe shape at different ash  
5 deposition times. Subsequently, the ash deposited FIVPEHs are comprehensively  
6 studied, including performance comparison, parameter analysis, and flow field  
7 analysis through wind tunnel experiments and CFD simulation.  
8  
9

## 10 **2. Design concepts and experiment setup**

### 11 **2.1 Design concepts**

12  
13  
14  
15  
16  
17  
18 During the combustion process, the high temperature in a furnace causes  
19 inorganic substances to undergo complex physical and chemical reactions, turning  
20 them into gases, liquids, and solids. All of them exist in the flue gas pipeline in the  
21 form of fly ash. Ash is formed due to the deposition of those inorganic materials in  
22 solid fuels after combustion [44]. When the flue gas flows through the heat exchanger,  
23 fly ash will deposit on the surface of the heat exchange tube. Because the fly ash in  
24 the flue gas pipe has a variety of physical states and the particle size of the ash  
25 particles ranges from nanometers to micrometers, there are several types of deposition  
26 mechanisms [45], including thermophoresis, inertial impaction, and eddy impaction.  
27 The ash deposition formed due to the first two mechanisms is usually located on the  
28 windward side of the tube. The ash deposition due to eddy impaction is often formed  
29 on the leeward side of the tube since the ash particles are too slight to separate from  
30 the flue gas flow and follow the airflow to the leeward side of the tube. Due to the  
31 eddy disturbance generated by the flow around the bluff body, the fly ash always  
32 deposits on the backside of the tube [46]. The schematic diagram of a general ash  
33 deposition process is shown in Fig. 1.  
34  
35  
36  
37  
38  
39  
40  
41  
42  
43  
44  
45  
46  
47  
48  
49  
50  
51  
52  
53  
54  
55  
56  
57  
58  
59  
60  
61  
62  
63  
64  
65

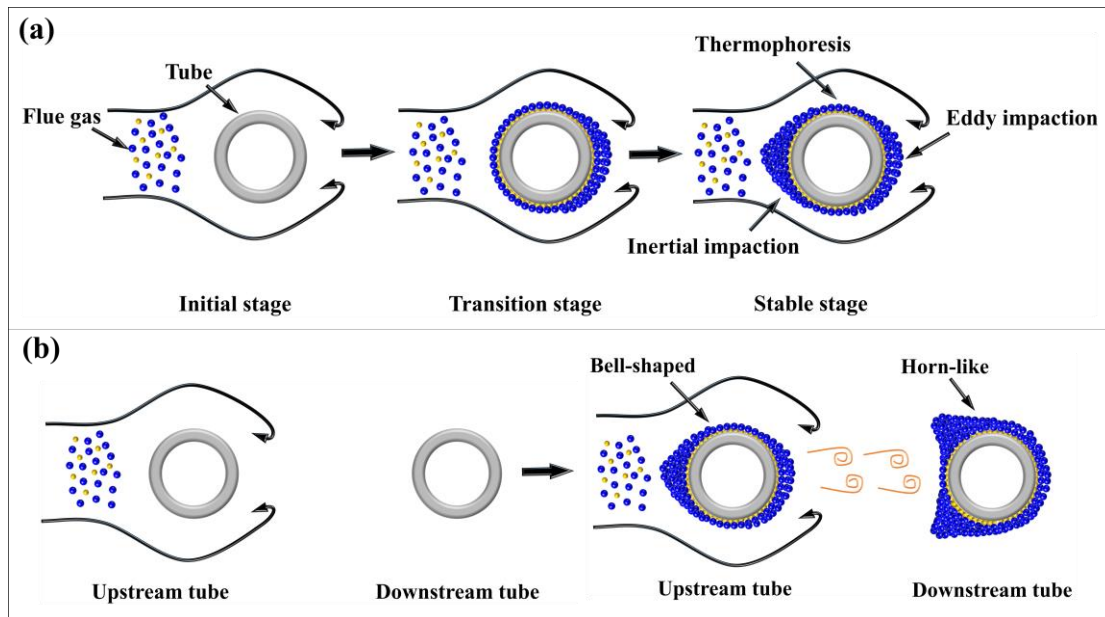


**Fig. 1.** (a) Schematic diagram of the three-stage process of ash deposition formation on a tube in heat exchange systems; (b) Schematic diagram of ash deposition shapes formed on multi-tubes in heat exchange systems.

Inspired by the deposition behavior of ash particles on the tube surface, this paper proposes to install a flow-induced piezoelectric energy harvester (FIVPEH) in the flue where aerokinetic energy exists. Ash deposition on the elliptic cylinder bluff body is considered, and its effect on the energy harvesting performance is investigated. Various shapes of ash depositions might lead to different aerodynamic characteristics of the bluff body. Therefore, two bluff bodies with differently shaped ash depositions are designed. Fig. 2 exhibits the schematic diagram of the two FIVPEHs with different ash deposition attached to the bluff bodies. According to the geometric profile, the bluff bodies presented in Fig. 2 (a) and (b) are referred to as bell-shaped and horn-like bluff bodies, respectively. According to the literature [44, 45], for a number tubes placed in series in the heat exchange system, the bell-shaped ash deposition is formed only on the first tube. Due to the influence of the wake of the upstream tube, horn-shaped ash depositions are formed on the remaining tubes. Both shapes of ash deposition are present in practice. In order to achieve a FIVPEH with a bell-shaped bluff body, one can install the FIVPEH in the front of all the tubes in the heat exchange system. To obtain a FIVPEH with a horn-shaped bluff body, one can install the FIVPEH at least after the first tube.

Each FIVPEH consists of a bluff body, a cantilever beam, and a piezoelectric transducer. The height of the bluff body is  $H$ . The length, width, and thickness of the cantilever beam are  $L$ ,  $W$ , and  $T_b$ , respectively. Fig. 2 (c) shows the key parameters that determine the geometric profiles of the bell-shaped and horn-like bluff bodies. Each bluff body is composed of a principal elliptic cylinder and one/two segmented ellipses. The segmented ellipse is an imitation of the ash deposition. The major and minor axes of the principal ellipse are  $a_1$  and  $b_1$ , and  $a_1 \times b_1 = 30 \text{ mm} \times 20 \text{ mm}$ . The major and minor axes of the segmented ellipse are  $a_2$  and  $b_2$ , and  $a_2 \times b_2 = 24 \text{ mm} \times 10 \text{ mm}$ . For the bell-shaped bluff body, the major axes of the principal ellipse and the

segmented ellipse are on the same horizontal line. The distance between the left ends of the two ellipses is  $d_1$ . Considering that ash deposition may gradually grow, four bell-shaped bluff bodies with different ash deposition sizes are investigated by increasing  $d_1$  from 3 mm to 12 mm with a step of 3 mm. For the horn-like bluff body, the two segmented ellipses are installed symmetrically on the two sides of the major axis of the principal ellipse. The angle between the major axes  $a_1$  and  $a_2$  is  $45^\circ$ . The distance from the end of the segmented ellipse to the edge of the principal ellipse is  $d_2$ . Similarly, four different  $d_2$  (3 mm, 6 mm, 9 mm, and 12 mm) are selected to simulate the ash deposition growth.

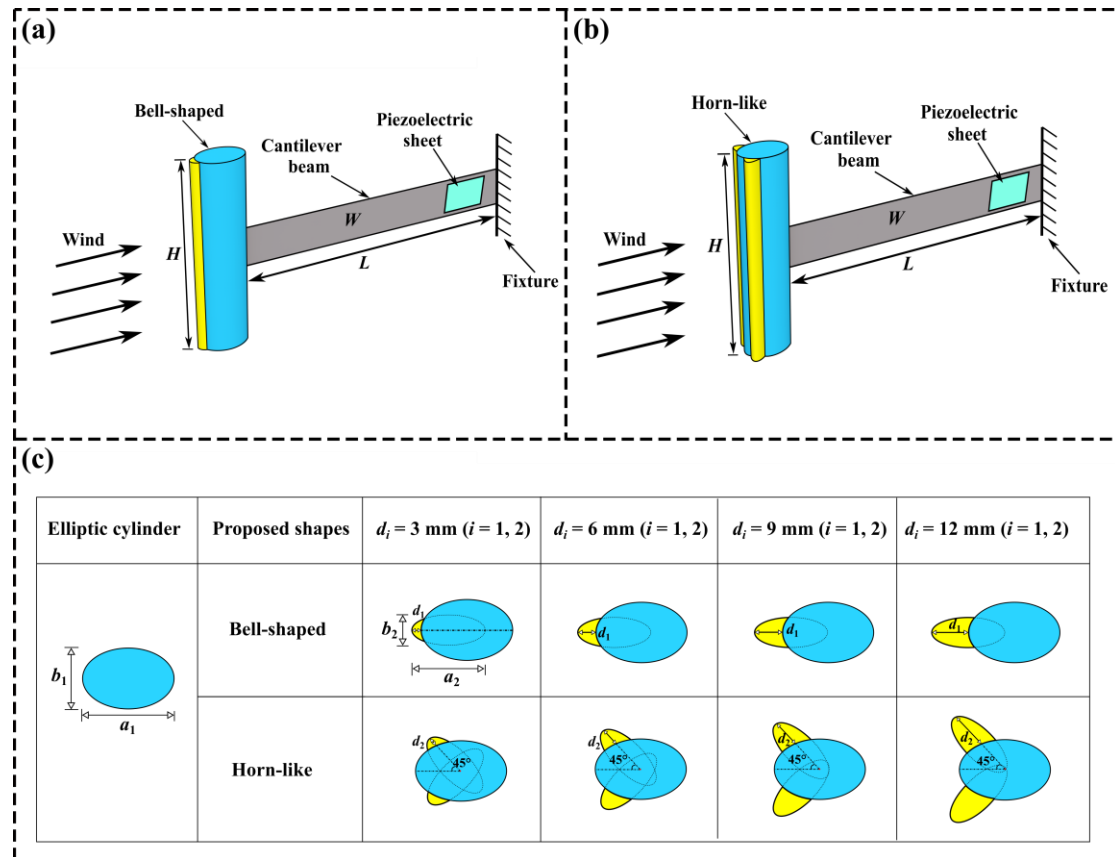
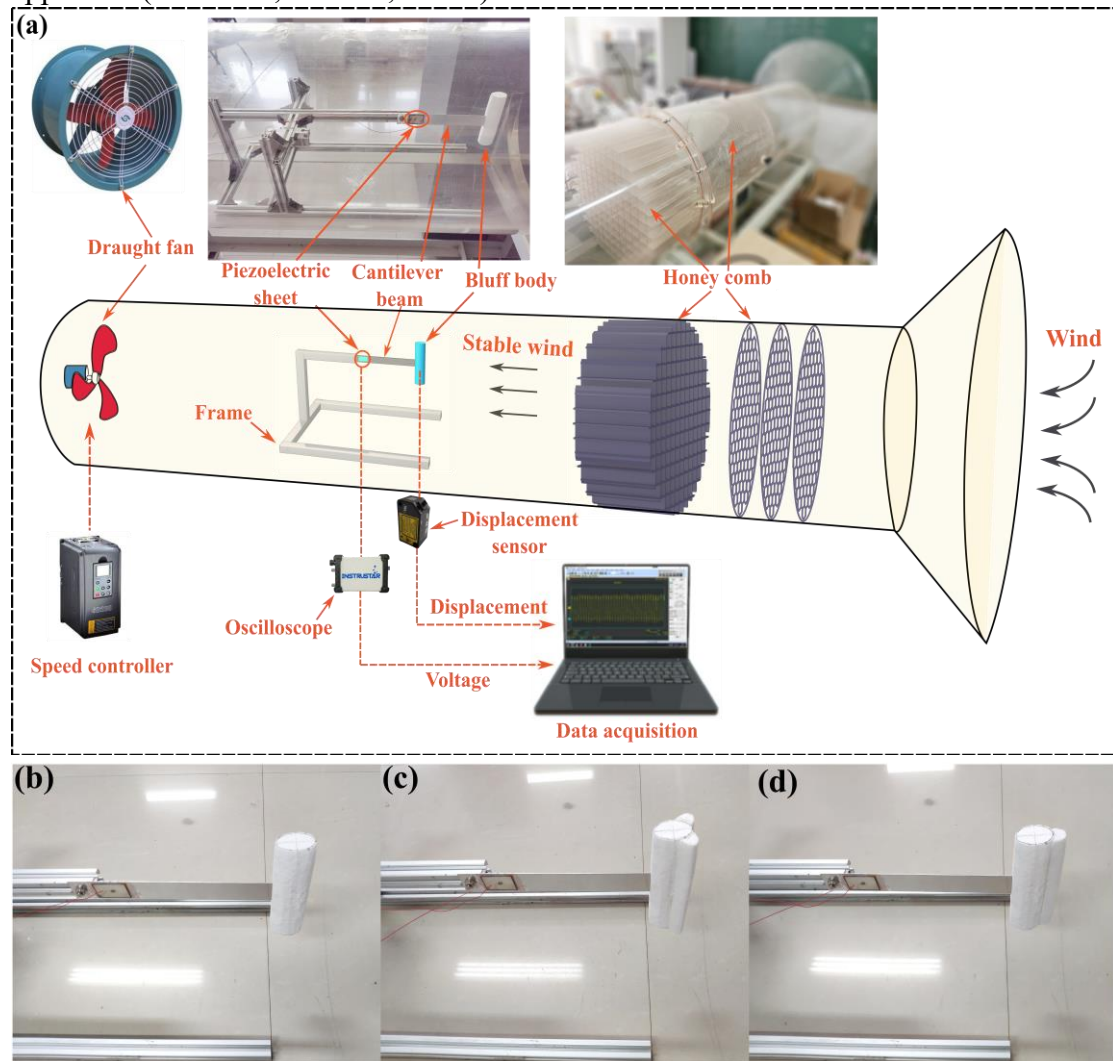


**Fig. 2.** Schematics of PEHs with different ash depositions: (a) bell-shaped ash deposition; (b) horn-like ash deposition; (c) geometries of the ash deposited bluff bodies.

## 2.2 Experimental setup

**Fig. 3** presents the experimental setup and the physical prototypes of the PEH with bell-shaped and horn-like bluff bodies. A PEH with an ordinary bluff body without ash deposition is used as the baseline model for comparison. In the experiment, the PEHs are, separately, placed in an open wind tunnel with a diameter of 400 mm. The turbulence intensity is controlled to be less than 1.0 %. The bluff body is made of rigid foam material. The major axis, the minor axis, and the height of the elliptic cylinder bluff body are 30 mm, 20 mm, and 118 mm, respectively. The cantilever beam is made of aluminum, and its dimensions are  $L \times W \times T_b = 184 \text{ mm} \times 25 \text{ mm} \times 0.5 \text{ mm}$ . The capacitance  $C_p$  of the piezoelectric transducer (PZT-5,

1 Jiaye-shi Co, China) is 24.87 nF. The wind speed in the wind tunnel is controlled by a  
 2 draught fan and is measured by a hot-wire anemometer (405i, Testo Company, USA).  
 3 The two-stage honeycomb device straightens the wind generated by the draught fan.  
 4 The wind speed range investigated in this paper is from 0.87 m/s to 3.61 m/s. The  
 5 natural frequencies of all the PEHs are calibrated to be almost the same,  
 6 approximately 8.0 Hz. The displacements of the bluff bodies are measured by a laser  
 7 displacement sensor (Panasonic: HG-C1400) with a resolution of 300  $\mu\text{m}$ . The signals  
 8 are recorded using a dual-channel USB data acquisition instrument (USB DAQ-280G).  
 9 The voltage generated by the piezoelectric transducer is recorded by a data acquisition  
 10 apparatus (DS1104S, RIGOL, China).  
 11  
 12  
 13



40  
41  
42  
43  
44  
45  
46  
47  
48  
49 **Fig. 3.** (a) The experimental setup; (b) the fabricated baseline PEH; (c) the fabricated PEH with  
 50 the horn-like bluff body; (d) the fabricated PEH with the bell-shaped bluff body.

### 51 52 53 3. Results and discussion

#### 54 55 56 57 3.1 The elliptic cylinder bluff body

58  
59  
60 The wind tunnel test results of the PEH with the elliptic cylinder bluff body are  
 61  
62  
63  
64  
65

illustrated in Fig. 4 and Fig. 5. Fig. 4 (a) and (b) present the output voltage and vibration amplitude responses, respectively. A lock-in region, with lower and upper bounds of 1.41 m/s and 2.51 m/s, is observed in the response diagram. It indicates that the PEH with the elliptic cylinder bluff body exhibits VIV. Over the lock-in region, with the increase of wind speed, the output voltage from the PEH first increases, then decreases. A maximum voltage of 2.33 V is obtained when the wind speed reaches 1.82 m/s. When the wind speed exceeds 2.51 m/s beyond the lock-in region, the voltage output becomes negligibly small. The displacement response of the PEH presented in Fig. 4 (b) exhibits a similar behavior. Appreciable vibration of the PEH occurs only within the lock-in region. The vibration amplitude reaches a maximum value of 7.06 mm at the wind speed of 2.51 m/s.

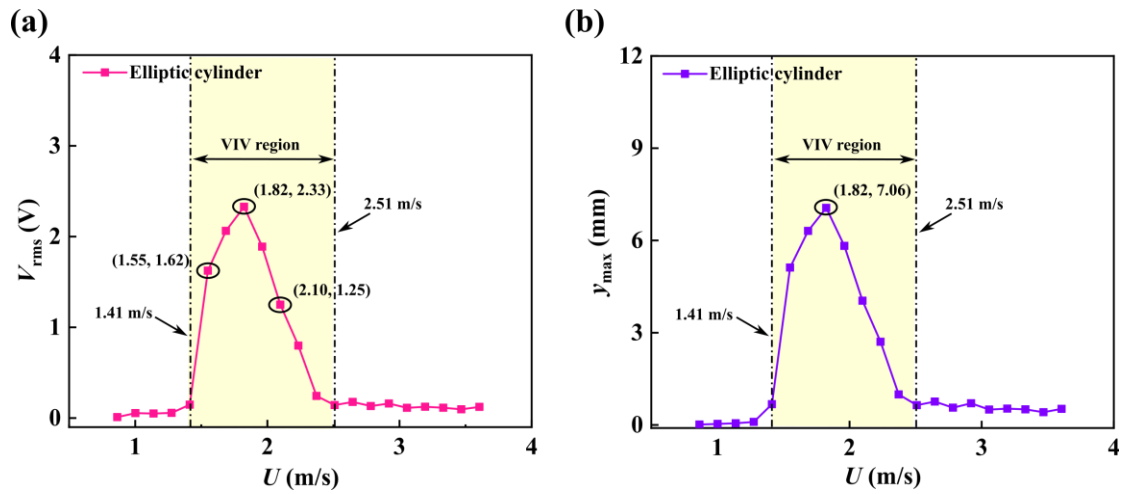
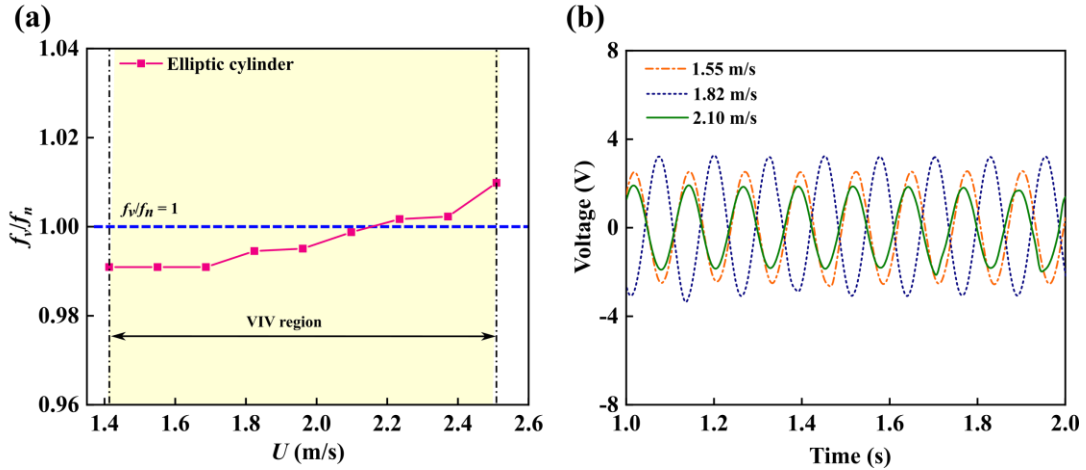


Fig. 4. Results of the PEH with elliptic cylinder bluff body: (a) RMS voltage output (b) maximum vibration displacement of the bluff body.

Fig. 5 exhibits the dominant vibration frequency of the PEH in the VIV region, and the voltage time-history is plotted at the wind speeds of 1.55 m/s, 1.82 m/s, and 2.10 m/s. The three wind speeds are, respectively, taken from the initial excitation branch, upper branch, and lower branch of the VIV region. In Fig. 5 (a), it is noted that the dimensionless frequency gradually increases to 1 as the wind speed increases, then keeps growing as the wind speed increases. However, the frequency shift in the lock-in region is minor, and the frequency ratio is always around 1. This phenomenon agrees with the results in the literature [47]. Thus, it further proves that the PEH with the elliptic cylinder bluff body performs VIV. It can be seen from Fig. 5 (b) that at all the three wind speeds, the PEH undergoes harmonic vibration. Due to the locking phenomenon, the output voltage of the PEH at the wind speed of 1.82 m/s is obviously larger than that when the wind speed is changed to 1.55 m/s or 2.10 m/s.



**Fig. 5.** (a) The dominant non-dimensional frequency of the PEH with elliptic cylinder bluff body under different wind speeds. (b) the voltage output time histories at the wind speeds 1.55 m/s, 1.82 m/s, and 2.10 m/s.

### 3.2 The Bell-shaped bluff body

As seen in **Fig. 6**, the bell-shaped additions produce a decrease in the amplitude of motion and a reduction of the voltage generated. For the PEH with the elliptic cylinder bluff body, the VIV phenomenon occurs over the wind speed range  $U = 1.41$  m/s  $\sim$  2.51 m/s. A maximum output voltage of 2.33 V is obtained at the wind speed of 1.82 m/s. For the PEH with the bell-shaped bluff body, for  $d_1$  equal to 3 mm, 6 mm, 9 mm, and 12 mm, the maximum voltage correspondingly becomes 0.99 V, 0.77 V, 0.44 V, and 0.49 V, and the maximum amplitude is 3.35 mm, 2.93 mm, 1.75 mm, and 1.79 mm, respectively. In other words, bell-shaped bluff bodies are not beneficial for energy harvesting. In contrast, they demonstrate the potential application for suppressing galloping-induced vibrations. Moreover, optimizing the parameters of the bell-shaped bluff body may lead to a maximum suppression performance. For instance, in the above case studies, the bell-shaped bluff body with  $d_1 = 9$  mm shows the strongest vibration suppression effect: its maximum amplitude is reduced by 75%, compared to the baseline model.

The time history responses of the PEH with the bell-shaped bluff body ( $d_1 = 9$  mm) at  $U = 1.41$  m/s are presented in **Fig. 6** (c) and (d). The results of the baseline model at  $U = 1.82$  m/s are also presented for comparison.  $U = 1.41$  m/s and 1.82 m/s are the optimal wind speeds to achieve the maximum voltage output for each case. Both cases exhibit harmonic vibration, while the baseline model has a significantly larger vibration amplitude, which is consistent with the results in **Fig. 6** (a) and (b).

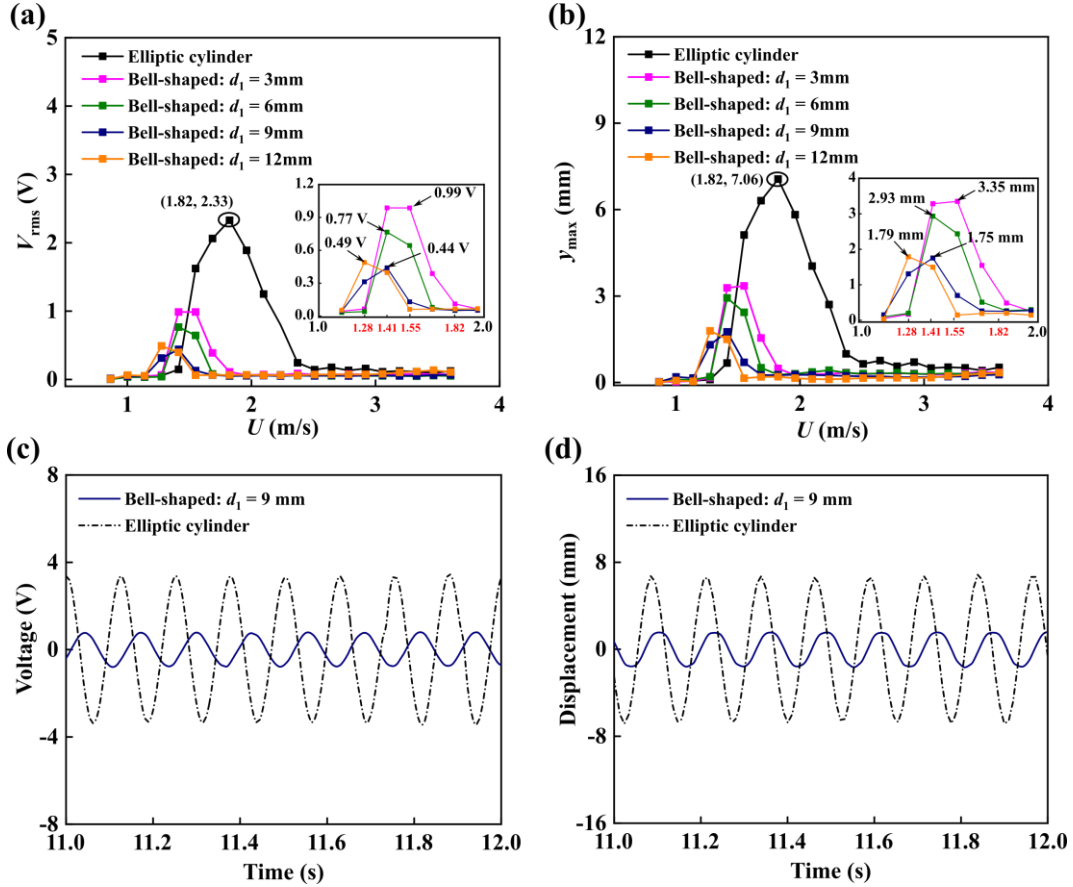


**Fig. 6.** Performance comparison of the PEHs with different bluff bodies: (a) RMS voltage outputs; (b) maximum vibration displacement of the bluff bodies; (c) time-history voltage output and (d) displacement of the PEHs with the bell-shaped bluff body under the optimal wind speed of  $U = 1.41$  m/s and the elliptic cylinder bluff body under the optimal wind speed of  $U = 1.82$  m/s.

### 3.3 The Horn-like bluff body

The results of the PEH with the horn-like bluff body of varying  $d_2$  are presented in **Fig. 7**. The results of the baseline model are also provided for comparison. **Fig. 7** (a) clearly shows that, unlike the baseline model, the PEH with the horn-like bluff body mainly exhibits the galloping phenomenon, regardless of the values of  $d_2$ . Hence, the PEH with the horn-like bluff body can produce significant voltage outputs over a much wider wind speed range. Moreover, unlike the behavior in the VIV region of the baseline model, with the increase of the wind speed, the voltage output monotonically increases. Over the wind speed range under investigation, for  $d_2$  equal to 3 mm, 6 mm, 9 mm, and 12 mm, the maximum voltage output of the PEH with the horn-like bluff body correspondingly becomes 14.06 V, 14.36 V, 14.20 V, and 14.24 V, which are much larger than that of the baseline model (2.33 V). **Fig. 7** (b) compares the displacement response of the PEH with the horn-like bluff body. For  $d_2$  equal to 3 mm, 6 mm, 9 mm, and 12 mm, the maximum displacement of the PEH with the horn-like bluff body becomes 49.96 mm, 56.32 mm, 54.45 mm, and 55.46 mm, which indicate 607%, 697%, 671%, and 685% **increases** compared to the baseline model. Among the

above cases, using the horn-like bluff body with  $d_2$  of 6 mm leads to the best performance. Its maximum voltage output is increased by 516% compared to the baseline model. In addition, the cut-in wind speed of the optimal design, i.e.,  $d_2 = 6$  mm, is about 1.28 m/s, which is smaller by 9% compared to the baseline model. Therefore, using the horn-like bluff body is also favorable for low wind speed energy harvesting.

In fact, the significant increase of the voltage output is the consequence of the galloping phenomenon. And the low cut-in wind speed advantage is inherited from the VIV behavior. In the enlarged views in Fig. 7 (a) and (b), it is noted that over the wind range 1.1 m/s  $\sim$  1.8 m/s, when  $d_2 = 3$  mm or 6 mm, the PEH with the horn-like bluff body undergoes VIV: the voltage/displacement response first increases, then decreases. When  $d_2 = 9$  mm or 12 mm, the VIV phenomenon appears in the wind speed range of 1.28 m/s  $\sim$  1.69 m/s. The time-history responses of the optimal design ( $d_2 = 6$  mm) at  $U = 1.82$  m/s, which is the optimal wind speed of the baseline model, are presented in Fig. 7 (c) and (d). It can be seen in Fig. 7 (a) that both cases exhibit harmonic vibration. Even  $U = 1.82$  m/s is the optimal wind speed of the baseline model, while not for the PEH with the horn-like bluff body; the voltage and displacement responses of the PEH with the horn-like bluff body are still larger than those of the baseline model. In brief, the PEH with the horn-like bluff body demonstrates a superior wind energy harvesting ability.

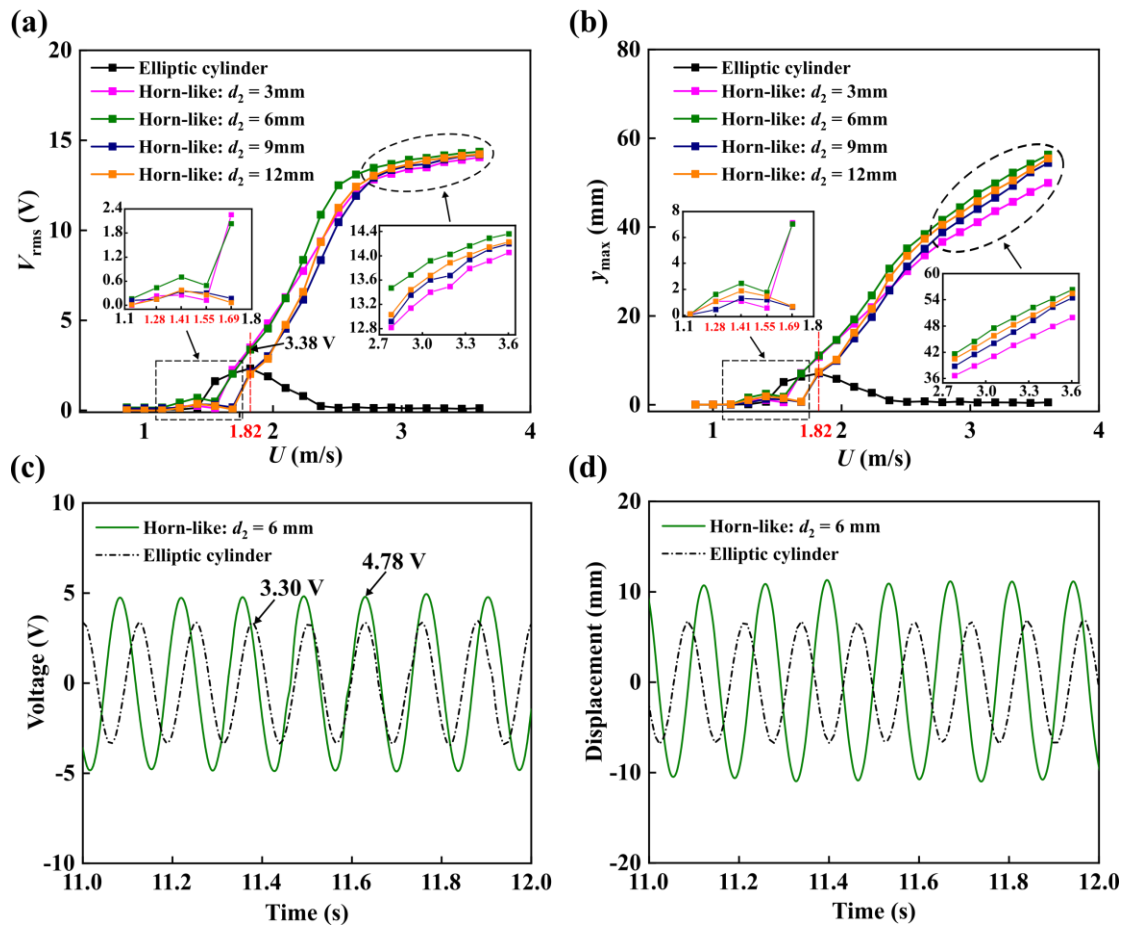


Fig. 7. Performance comparison of the PEHs with different bluff bodies: (a) RMS voltage outputs;



(b) maximum vibration displacement of the bluff bodies; (c) time-history voltage output and (d) displacement of the PEHs with the horn-like bluff body and the elliptic cylinder bluff body under the wind speed of  $U = 1.82$  m/s.

#### 4. Interpretation based on CFD simulation

Computational fluid dynamics (CFD) simulations are carried out to further reveal the effect of ash deposition on the aerodynamics of the bluff body. CFD models are built using the commercial software XFlow, which adopts the lattice Boltzmann method. The dimensions of the bluff bodies in simulations are consistent with those of the physical prototypes tested in the experiments. The calculation domain set in the simulation is a rectangle with a length of  $40b_1$  and a width of  $20b_1$ , where  $b_1$  is the length of the minor axis of the principal ellipse of the bluff body. The left and right boundary conditions of the calculation domain are set as velocity inlet and flow outlet, respectively. The fluid is air. The upper and lower boundary conditions are set to be walls. The distance between the center of the bluff body and the upper boundary is  $10b_1$ , and that to the outlet boundary is  $30b_1$  to ensure that the flow field behind the bluff body can be fully developed. In the CFD simulations, the external single-phase forced incompressible model is selected to simulate the flow. The time step is automatically fixed to  $5 \times 10^{-5}$  s. The Reynolds number of the simulated flow field is approximately 2460.

As known from the results presented in the previous section, using the bell-shaped bluff body leads to vibration suppression and a deteriorated energy harvesting performance. On the contrary, using the horn-like bluff body induces the galloping phenomenon and significantly improves the energy harvesting performance. **Fig. 8** presents the vorticity contours of the bell-shaped ( $d_1 = 9$  mm), elliptic cylinder, and horn-like ( $d_2 = 6$  mm) bluff bodies at different time stages to reveal the aerodynamic mechanisms behind the above conclusion. From **Fig. 8**, one can find that for the bell-shaped bluff body, the presence of a small elliptical bulge in the front streamlines the oncoming flow over the bluff body. Thus, the vortex shedding is similar to that of the elliptic cylinder bluff body: in both cases, primary large-scale vortices (PV) are produced behind the bluff bodies. The width of the wake is evaluated to indicate the intensity of the vortex shedding. The widths of the wake produced after the bell-shaped and elliptic cylinder bluff bodies are  $1.57b_1$  and  $1.79 b_1$ , respectively. **This** implies that the intensity of the vortex shedding of the bell-shaped bluff body is weaker than that of the elliptic cylinder. This explains why the vibration amplitude of the bell-shaped bluff body is smaller than that of the elliptic cylinder one. Unlike the elliptic cylinder bluff body, for the horn-like one, due to the presence of two small elliptical bulges, not only primary large-scale vortices (PV), but also small-scale secondary vortices (SV) are produced in the wake flow. Because of the interaction between PV and SV, the vortex shedding effect is delayed, resulting in a significant increase of the wake vortices. Moreover, it is observed that the wake width of the horn-like bluff body is much wider than that of the elliptic cylinder one, which indicates a stronger aerodynamic instability in the wake. Therefore, unlike the

vibration mode of the elliptic cylinder bluff body, the vibration mode of the horn-like bluff body is galloping, which can induce a larger-amplitude vibration and produce a higher voltage output. In summary, the formation of small-scale secondary vortices (SV) plays a key role in the intensity of vibration.

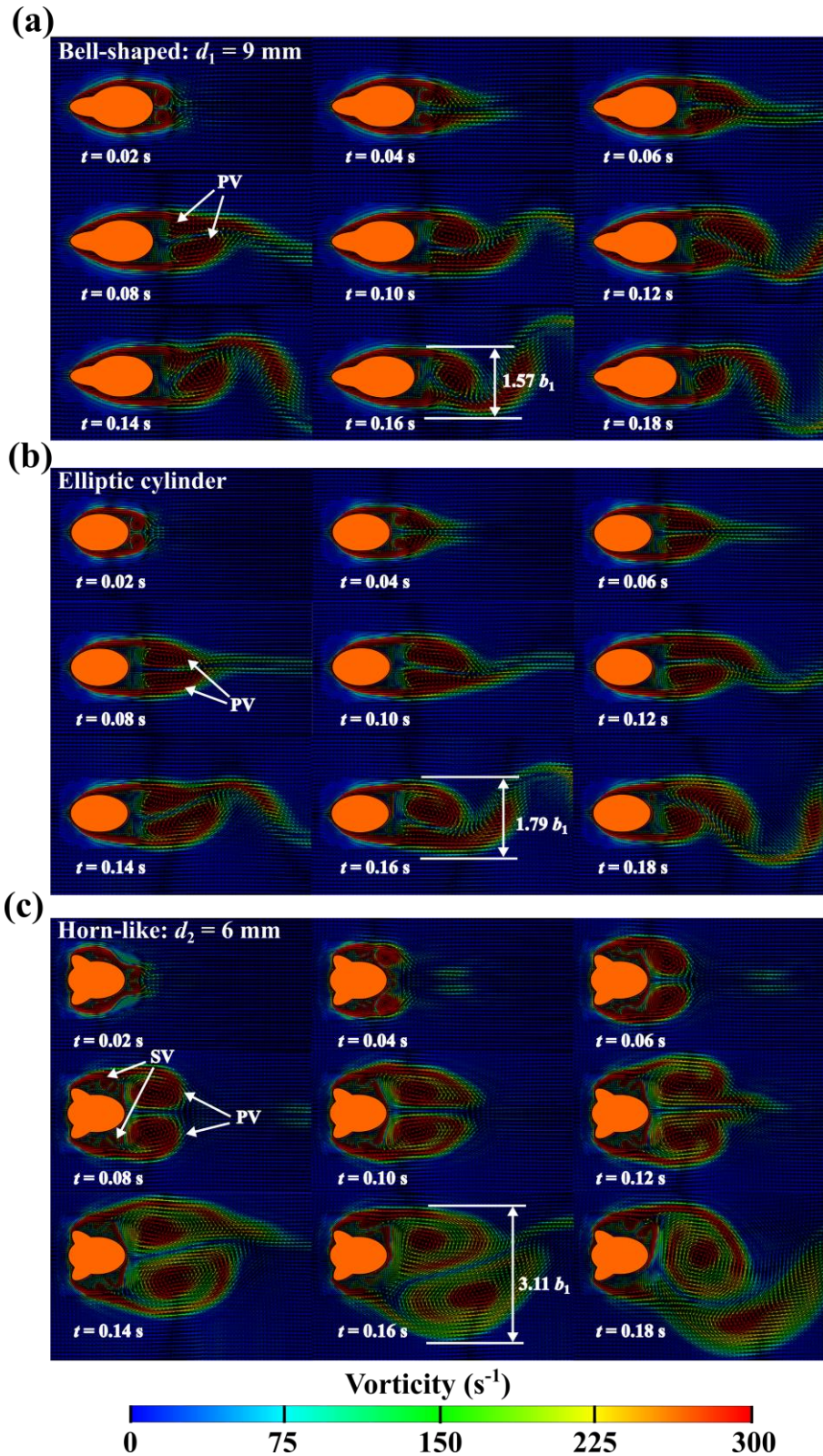
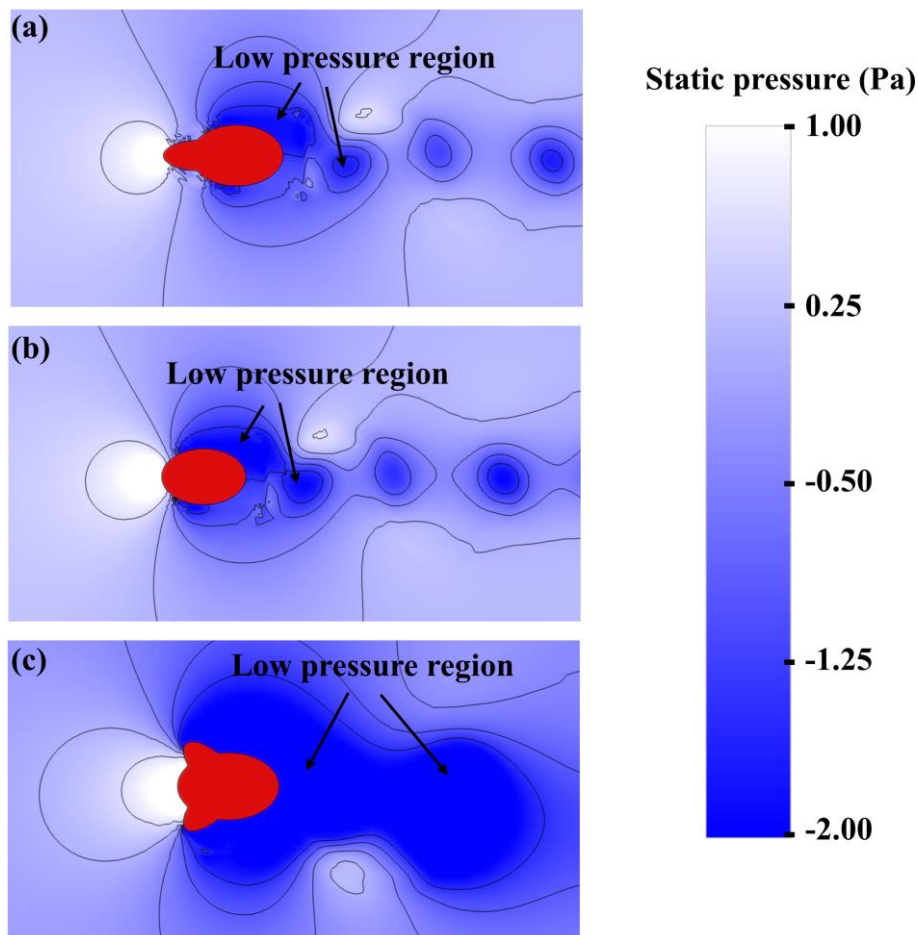


Fig. 8. Comparison of flow-field evolution with time for the three bluff bodies at the wind speed

of  $U = 1.82$  m/s: (a) the bell-shaped ( $d_1 = 9$  mm) bluff body; (b) the elliptic cylinder bluff body; (c) the horn-like ( $d_2 = 6$  mm) bluff body.

The pressure contours around the bell-shaped ( $d_1 = 9$  mm), elliptic cylinder, and horn-like ( $d_2 = 6$  mm) bluff bodies at the wind speed of 1.82 m/s are shown in **Fig. 9**. Obviously, it can be observed that the low-pressure region around the horn-like bluff body is significantly larger than those around the other two bluff bodies. The larger pressure difference causes the horn-like bluff body to vibrate more violently than the other two bluff bodies. Comparing the bell-shaped and elliptic cylinder bluff bodies, the low-pressure region around the bell-shaped bluff body is smaller than that around the elliptic cylinder bluff body. Therefore, the bell-shaped bluff body undergoes the smallest vibration. **Fig. 10** presents the velocity contours of the bell-shaped ( $d_1 = 9$  mm), elliptic cylinder, and horn-like ( $d_2 = 6$  mm) bluff bodies at the wind speed of 1.82 m/s. The high-velocity region in **Fig. 10** corresponds to the low-pressure region in **Fig. 9**. The high-velocity region around the horn-like bluff body is the largest, which enhances the oscillation of the horn-like bluff body, and makes its vibration significantly higher than the other two bluff bodies. The above discussion agrees well with the conclusions obtained from the experiments in the previous section.



**Fig. 9.** Pressure contour around (a) the bell-shaped ( $d_1 = 9$  mm) bluff body; (b) the elliptic cylinder bluff body; (c) the horn-like ( $d_2 = 6$  mm) bluff body at the wind speed of 1.82 m/s.

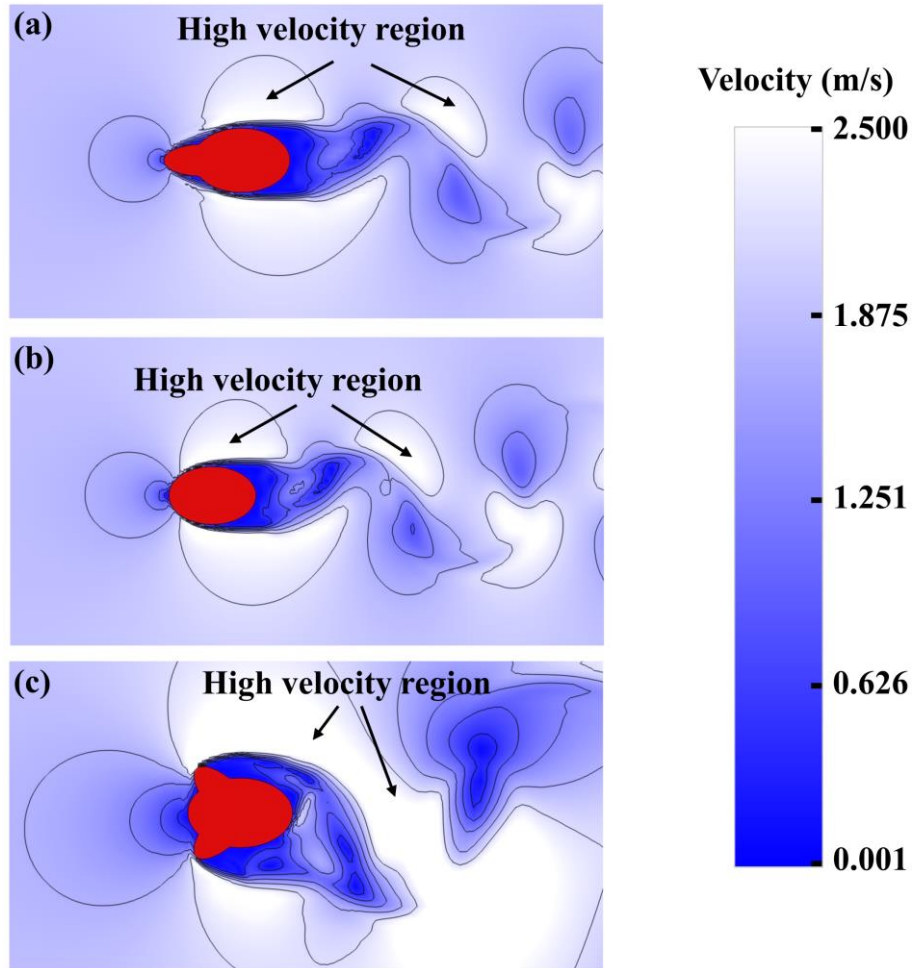


**Fig. 10.** Velocity contour around (a) the bell-shaped ( $d_1 = 9$  mm) bluff body; (b) the elliptic cylinder bluff body; (c) the horn-like ( $d_2 = 6$  mm) bluff body at the wind speed of 1.82 m/s.

## 5. Conclusion

This paper has explored the effect of ash deposition on flow-induced vibration energy harvesting in heat exchange systems. According to the shape and size of ash deposition, bell-shaped and horn-like bluff bodies have been proposed to simulate different ash depositions. Experimental results have revealed that the bell-shaped bluff bodies can suppress vibrations and are not beneficial for energy harvesting. In contrast, the horn-like bluff bodies can improve the energy harvesting performance by transforming VIV to galloping. The combination of VIV and galloping reduces the cut-in wind speed of the PEH and increases the voltage outputs under high wind speeds. The voltage output of an optimal prototype with  $d_2 = 6$  mm has been increased by 516%. Besides, CFD simulations have been conducted to interpret the underlying mechanisms behind the phenomena. For the bell-shaped bluff body, a weaker aerodynamic force is generated because the wake width is smaller than that of the elliptic cylinder bluff body. Thus, the vibration of the bluff body is **diminished**. For the horn-like bluff body, due to the interaction of PV and SV, the wake width is increased, resulting in an increased aerodynamic force. The flow-induced vibration

1 transforms from VIV to galloping. Therefore, a larger voltage output is generated by  
2 the PEH with the horn-like bluff body. In summary, a potential usefulness of the  
3 harmful ash deposition phenomenon in the flue gas pipeline for benefiting energy  
4 harvesting has been proposed and explored. Different ash deposition effects have been  
5 investigated. The work presented in this paper represents a preliminary study of the  
6 ash deposition effect on flow-induced vibration energy harvesting.  
7  
8  
9

## 10 Acknowledgments

11  
12 This work was supported by the National Natural Science Foundation of China  
13 (Grant No. 51977196), the China Postdoctoral Science Foundation (Grant No.  
14 2020T130557), the Natural Science Foundation of Excellent Youth of Henan Province  
15 (Grant No. 222300420076), and the State Key Laboratory of Structural Analysis for  
16 Industrial Equipment, Dalian University of Technology, China (GZ21114).  
17  
18  
19  
20

## 21 References

- 22  
23  
24 [1] J. Wang, L. Geng, L. Ding, H. Zhu, D. Yurchenko, The state-of-the-art review on energy harvesting  
25 from flow-induced vibrations, *Appl. Energy*, 267 (2020) 114902.  
26  
27 [2] X.W. Fu, Y.S. Yang, Modeling and analysis of cascading node-link failures in multi-sink wireless  
28 sensor networks, *Reliab. Eng. Syst. Saf.*, 197 (2020) 15.  
29  
30 [3] Z. Lai, S. Wang, L. Zhu, G. Zhang, J. Wang, K. Yang, D. Yurchenko, A hybrid piezo-dielectric wind  
31 energy harvester for high-performance vortex-induced vibration energy harvesting, *Mech. Syst. Signal.*  
32 *Process.*, 150 (2021).  
33  
34 [4] C. Magazzino, M. Mele, N. Schneider, A machine learning approach on the relationship among  
35 solar and wind energy production, coal consumption, GDP, and CO2 emissions, *Renew. Energ.*, 167  
36 (2021) 99-115.  
37  
38 [5] J.J. Yoo, G. Seo, M.R. Chua, T.G. Park, Y.L. Lu, F. Rotermund, Y.K. Kim, C.S. Moon, N.J. Jeon, J.P.  
39 Correa-Baena, V. Bulovic, S.S. Shin, M.G. Bawendi, J. Seo, Efficient perovskite solar cells via  
40 improved carrier management, *Nature*, 590 (2021) 10.  
41  
42 [6] C.H. Li, S.C. Xu, J. Yu, Z. Li, W.F. Li, J.H. Wang, A.H. Liu, B.Y. Man, S.K. Yang, C. Zhang, Local  
43 hot charge density regulation: Vibration-free pyroelectric nanogenerator for effectively enhancing  
44 catalysis and in-situ surface enhanced Raman scattering monitoring, *Nano Energy*, 81 (2021) 10.  
45  
46 [7] J.L. Wang, S.H. Gu, C.Y. Zhang, G.B. Hu, G. Chen, K. Yang, H. Li, Y.Y. Lai, G. Litak, D.  
47 Yurchenko, Hybrid wind energy scavenging by coupling vortex-induced vibrations and galloping,  
48 *Energy Convers. Manag.*, 213 (2020) 11.  
49  
50 [8] T. Morbiato, C. Borri, R. Vitaliani, Wind energy harvesting from transport systems: A resource  
51 estimation assessment, *Appl. Energy*, 133 (2014) 152-168.  
52  
53 [9] M.A. Mustapa, O.B. Yaakob, Y.M. Ahmed, C.K. Rheem, K.K. Koh, F.A. Adnan, Wave energy  
54 device and breakwater integration: A review, *Renew. Sust. Energ. Rev.*, 77 (2017) 43-58.  
55  
56 [10] C. Chen, Z.Y. Liu, S.H. Wan, J.T. Luan, Q.Q. Pei, Traffic Flow Prediction Based on Deep  
57 Learning in Internet of Vehicles, *IEEE Trans. Intell. Transp. Syst.*, 22 (2021) 3776-3789.  
58  
59 [11] H.S. Kim, J.-H. Kim, J. Kim, A review of piezoelectric energy harvesting based on vibration,  
60 *International Journal of Precision Engineering and Manufacturing*, 12 (2011) 1129-1141.  
61  
62  
63  
64  
65

- 1 [12] F.K. Shaikh, S. Zeadally, Energy harvesting in wireless sensor networks: A comprehensive review,  
2 *Renew. Sust. Energ. Rev.*, 55 (2016) 1041-1054.
- 3 [13] S. Fang, X. Fu, X. Du, W.-H. Liao, A music-box-like extended rotational plucking energy  
4 harvester with multiple piezoelectric cantilevers, *Applied Physics Letters*, 114 (2019).
- 5 [14] X. Zhao, J. Cai, Y. Guo, C. Li, J. Wang, H. Zheng, Modeling and experimental investigation of an  
6 AA-sized electromagnetic generator for harvesting energy from human motion, *Smart. Mater. Struct.*,  
7 27 (2018).
- 8 [15] K. Fan, Y. Zhang, S. E. L. Tang, H. Qu, A string-driven rotor for efficient energy harvesting from  
9 ultra-low frequency excitations, *Appl. Phys. Lett.*, 115 (2019).
- 10 [16] Z. Yang, L. Tang, L. Yu, K. Tao, K. Aw, Modelling and analysis of an out-of-plane electret-based  
11 vibration energy harvester with AC and DC circuits, *Mech. Syst. Signal. Process.*, 140 (2020).
- 12 [17] G. Hu, C. Zhao, Y. Yang, X. Li, J. Liang, Triboelectric energy harvesting using an origami-inspired  
13 structure, *Appl. Energy*, 306 (2022) 118037.
- 14 [18] J. Wang, S. Zhou, Z. Zhang, D. Yurchenko, High-performance piezoelectric wind energy harvester  
15 with Y-shaped attachments, *Energy Conversion and Management*, 181 (2019) 645-652.
- 16 [19] A. Abdelkefi, Aeroelastic energy harvesting: A review, *International Journal of Engineering  
17 Science*, 100 (2016) 112-135.
- 18 [20] L.B. Zhang, H.L. Dai, A. Abdelkefi, L. Wang, Improving the performance of aero elastic energy  
19 harvesters by an interference cylinder, *Appl. Phys. Lett.*, 111 (2017).
- 20 [21] K. Yang, T. Qiu, J. Wang, L. Tang, Magnet-induced monostable nonlinearity for improving the  
21 VIV-galloping-coupled wind energy harvesting using combined cross-sectioned bluff body, *Smart  
22 Materials and Structures*, 29 (2020).
- 23 [22] K. Yang, J.L. Wang, D. Yurchenko, A double-beam piezo-magneto-elastic wind energy harvester  
24 for improving the galloping-based energy harvesting, *Appl. Phys. Lett.*, 115 (2019) 5.
- 25 [23] A. Abdelkefi, A.H. Nayfeh, M.R. Hajj, Modeling and analysis of piezoaeroelastic energy  
26 harvesters, *Nonlinear Dyn.*, 67 (2011) 925-939.
- 27 [24] M. Bryant, E. Garcia, Modeling and Testing of a Novel Aeroelastic Flutter Energy Harvester,  
28 *Journal of Vibration and Acoustics-Transactions of the Asme*, 133 (2011) 011010.
- 29 [25] H. Wang, W. Yang, K.D. Nguyen, G. Yu, Wake-induced vibrations of an elastically mounted  
30 cylinder located downstream of a stationary larger cylinder at low Reynolds numbers, *Journal of Fluids  
31 and Structures*, 50 (2014) 479-496.
- 32 [26] H.D. Akaydin, N. Elvin, Y. Andreopoulos, The performance of a self-excited fluidic energy  
33 harvester, *Smart. Mater. Struct.*, 21 (2012).
- 34 [27] H.L. Dai, A. Abdelkefi, L. Wang, Theoretical modeling and nonlinear analysis of piezoelectric  
35 energy harvesting from vortex-induced vibrations, *J. Intell. Mater. Syst. Struct.*, 25 (2014) 1861-1874.
- 36 [28] V. Azadeh-Ranjbar, N. Elvin, Y. Andreopoulos, Vortex-induced vibration of finite-length circular  
37 cylinders with spanwise free-ends: Broadening the lock-in envelope, *Physics of Fluids*, 30 (2018).
- 38 [29] G. Hu, K.T. Tse, M. Wei, R. Naseer, A. Abdelkefi, K.C.S. Kwok, Experimental investigation on  
39 the efficiency of circular cylinder-based wind energy harvester with different rod-shaped attachments,  
40 *Appl. Energy*, 226 (2018) 682-689.
- 41 [30] J.L. Wang, S.K. Sun, L.H. Tang, G.B. Hu, J.R. Liang, On the use of metasurface for  
42 Vortex-Induced vibration suppression or energy harvesting, *Energy Convers. Manag.*, 235 (2021) 14.
- 43 [31] J.P.D. Hartog, Transmission line vibration due to sleet, *Transactions of the American Institute of  
44 Electrical Engineers*, 51 (1932) 1074-1076.
- 45  
46  
47  
48  
49  
50  
51  
52  
53  
54  
55  
56  
57  
58  
59  
60  
61  
62  
63  
64  
65

- 1 [32] C. Scruton, Wind effects on structures, James Clayton Lecture, Proceedings Institution of  
2 Mechanical Engineers, 185 (1971) 301-317.
- 3 [33] G.V. Parkinson, Wind-induced instability of structures, Philosophical Transactions of the Royal  
4 Society of London, A269 (1971) 395-409.
- 5 [34] G.V. Parkinson, Phenomena and modelling of flow-induced vibrations of bluff bodies, Progress in  
6 Aerospace Sciences, 26 (1989) 169-224.
- 7 [35] R.D. Blevins, Flow-Induced Vibration, Van Nostrand Reinhold, New York, 1990.
- 8 [36] M.P. Paidoussis, S.J. Price, E. De Langre, Fluid-structure interactions: cross-flow-induced  
9 instabilities, Cambridge University Press, 2010.
- 10 [37] A. Barrero-Gil, G. Alonso, A. Sanz-Andres, Energy harvesting from transverse galloping, J. Sound  
11 Vibr., 329 (2010) 2873-2883.
- 12 [38] J. Sirohi, R. Mahadik, Harvesting Wind Energy Using a Galloping Piezoelectric Beam, Journal of  
13 Vibration and Acoustics-Transactions of the Asme, 134 (2012).
- 14 [39] A. Abdelkefi, M.R. Hajj, A.H. Nayfeh, Power harvesting from transverse galloping of square  
15 cylinder, Nonlinear Dynamics, 70 (2012) 1355-1363.
- 16 [40] J. Wang, S. Sun, G. Hu, Y. Yang, L. Tang, P. Li, G. Zhang, Exploring the potential benefits of  
17 using metasurface for galloping energy harvesting, Energy Convers. Manag., 243 (2021).
- 18 [41] H. Han, Y.-L. He, W.-Q. Tao, Y.-S. Li, A parameter study of tube bundle heat exchangers for  
19 fouling rate reduction, International Journal of Heat and Mass Transfer, 72 (2014) 210-221.
- 20 [42] D. Bouris, E. Konstantinidis, S. Balabani, D. Castiglia, G. Bergeles, Design of a novel, intensified  
21 heat exchanger for reduced fouling rates, International Journal of Heat and Mass Transfer, 48 (2005)  
22 3817-3832.
- 23 [43] S.G. Mavridou, D.G. Bouris, Numerical evaluation of a heat exchanger with inline tubes of  
24 different size for reduced fouling rates, International Journal of Heat and Mass Transfer, 55 (2012)  
25 5185-5195.
- 26 [44] S.-Z. Tang, Y.-L. He, F.-L. Wang, Y.-B. Tao, Parametric study on fouling mechanism and heat  
27 transfer characteristics of tube bundle heat exchangers for reducing fouling considering the deposition  
28 and removal mechanisms, Fuel, 211 (2018) 301-311.
- 29 [45] Y. Cai, K. Tay, Z. Zheng, W. Yang, H. Wang, G. Zeng, Z. Li, S. Keng Boon, P. Subbaiah, Modeling  
30 of ash formation and deposition processes in coal and biomass fired boilers: A comprehensive review,  
31 Appl. Energy, 230 (2018) 1447-1544.
- 32 [46] S.-Z. Tang, M.-J. Li, F.-L. Wang, Z.-B. Liu, Fouling and thermal-hydraulic characteristics of  
33 aligned elliptical tube and honeycomb circular tube in flue gas heat exchangers, Fuel, 251 (2019)  
34 316-327.
- 35 [47] Navrose, S. Mittal, Lock-in in vortex-induced vibration, Journal of Fluid Mechanics, 794 (2016)  
36 565-594.
- 37  
38  
39  
40  
41  
42  
43  
44  
45  
46  
47  
48  
49  
50  
51  
52  
53  
54  
55  
56  
57  
58  
59  
60  
61  
62  
63  
64  
65

**Declaration of interests**

The authors declare that they have no known competing financial interests or personal relationships that could have appeared to influence the work reported in this paper.

The authors declare the following financial interests/personal relationships which may be considered as potential competing interests: